

UNIVERSITY OF TARTU
FACULTY OF SCIENCE AND TECHNOLOGY
Institute of Physics

GRIGORI SAVUSTJAN

**Comparison of Foucault cardiogram with
MRI ventricular volume-time curve**

MASTER'S THESIS
IN
APPLIED PHYSICS

Supervisor: Docent Jüri Vedru, Ph.D.

TARTU 2010

ACKNOWLEDGEMENTS

This work has been done as thesis for master degree from the University of Tartu. I would like to acknowledge all people who had helped me during my work on present thesis. Especially, I would like to thank my supervisor Associate Professor Ph. D. Jüri Vedru. He has been really helpful and his advices and good ideas during interesting discussions were at most required and inspiring.

The study on present thesis has been done at West Tallinn Central Hospital. I would like to thank Head of Radiology Department M.D. Eve Toomik and Medical Physicist M. Sc. Juri Nosach for helping me with conduction of cardiac MRI study at the hospital. Their contribution to this thesis is invaluable. I would like to thank M.D. Ilja Lapidus also for the very interesting discussion about heart mechanical activity and its measurements from medical doctor's perspective.

I want to express my deepest gratitude to my family and friends, who have been always very supportive and encouraging about my work on my master's thesis.

ABSTRACT

Monitoring of mechanical parameters of the heart provides essential information to medical doctors for patient health assessment. There is a lack of cheap and robust method for continuous monitoring of these parameters. Currently used methods do allow neither automation nor continuous monitoring without skilled operators.

Purpose of the current thesis is to assess possibility of using Foucault cardiography for monitoring mechanical parameters of the heart at the hospital, by comparing Foucault cardiogram with the volume-time curve, obtained from segmented cardiac MRI images. In the present work we develop a method for detection of heart in images and propose an *active contours* method as the base for automatic segmentation of these images. We introduce novel algorithms for post segmentation processing and cleaning of segmented images. For computational purposes and various algorithm implementations MATLAB 2010 with the Spline and Image Processing toolboxes have been used.

Keywords: Foucault cardiogram, induction cardiogram, electrical bioimpedance, magnetic resonance imaging, heart activity, ventricular volume cycle, comparison of waveforms, image processing, signal processing, active contours

Märksõnad: Foucault' kardiogramm, induktsiooni kardiogramm, elektriline bioimpedants, MRT, südame tegevus, vatsakeste ruumala kõver, lainekuju võrdlemine, pilditöötlus, signaalitöötlus, aktiivsed kontuurid.

CONTENTS

1	PROBLEM REVIEW.....	6
1.1	Foucault cardiography.....	6
1.2	Foucault cardiogram waveforms.....	8
1.3	Medical imaging techniques available for tracking cardiac activity.....	11
1.4	Previous work done on determining heart ventricular volume with commonly used medical imaging techniques.....	12
1.5	Statement of the problem.....	15
2	MATERIALS AND METHODS.....	16
2.1	Signa HDx 1.5T MRI system.....	16
2.2	GE LOGIQ 3 ultrasound system.....	17
2.3	Foucault cardiography device.....	17
2.4	DICOM file format.....	18
2.5	Signal processing methods.....	19
2.6	Digital image processing methods.....	23
2.7	Active contours as method for image segmentation.....	25
2.8	Splines for curve fitting.....	26
2.9	Similarity index between waveforms.....	27
3	DESCRIPTION OF WORK DONE.....	28
3.1	MRI research planning and conduction conditions.....	28
3.2	Ultrasound measurement of cardiac ejection fraction.....	32
3.3	Foucault cardiogram recording.....	32
3.4	Image processing algorithm.....	33
3.5	Manual segmentation of MRI images.....	43
3.6	Foucault cardiogram processing.....	44
4	DISCUSSION AND RESULT ANALYSIS.....	46
4.1	Manual versus active contour segmentation of MRI images.....	46
4.2	Comparison of ejection fractions obtained from MRI and Ultrasound.....	47
4.3	Volume-time curve from segmented MRI images versus FouCG averaged waveform.....	48
4.4	Future efforts.....	53
5	CONCLUSIONS.....	54

6	SUMMARY.....	55
7	KOKKUVÕTE.....	56
8	BIBLIOGRAPHY.....	57
9	APPENDICES.....	61
9.1	MATLAB program code (on a compact disc).....	61
9.2	Processed images.....	62
9.3	Figures.....	67
9.4	Glossary.....	71

1 PROBLEM REVIEW

1.1 Foucault cardiography

Medical diagnostic requires automated methods for continuous monitoring of principal bio-mechanical parameters of the heart. The most important of these parameters are heart ejection fraction (the fraction of blood pumped out of ventricles with each heart beat), stroke volume and cardiac output. Continuous monitoring of heart bio-mechanical parameters provides cardiologists with essential information about its current state.

Usage of existing medical devices for the heart diagnostics can sometimes be expensive and requires experienced technicians for proper operation. Possible solution for this problem lies in development of cheap and informative method of diagnostics.

In the year 1965 early work started on non-invasive method for probing human body at the University of Tartu, but since any references to compare obtained signal with were absent, further research on this topic has been ceased and forgotten for decades.

Independently from the University of Tartu similar research has been conducted in the United States. Since it is known that the heart pumps blood through the body, and lungs are filled with air during breathing, the volume of organs changes rapidly over time. Effect of these two mechanical actions can be described as redistribution of well conducting blood and poor conducting air inside the chest. As shown by Tarjan [2], the measurement system based on magnetic induction is able to monitor heart and lung signals in the human body. This method was called magnetic induction cardiography by the researchers.

Since 1994 research on this impedance method has been resumed at the University of Tartu [1], [4]. The research group denominated method as Foucault cardiography in honour of French physicist Léon Foucault who had studied eddy currents. Foucault cardiography claims to be the candidate for continuous monitoring of the heart mechanical activity. It is based on the absorption of high frequency eddy currents induced by magnetic field in thoracic region [6]. The absorbed power depends on the blood and air contents in the tissues and thus it varies with changes in shape and volume of the organs located close to the source of the inducting field.

The device able to conduct measurements has been constructed. It consists of single-turn inductor coil made of copper strap, being 135 mm in diameter and capacitor connected in parallel. The inductor and capacitor form a resonant circuit of a 7.7 MHz autonomous LC generator and serve as a sensor of the Foucault cardiograph. Mean voltage amplitude on the inductor is stabilized to 1.1 V, corresponding current in the coil is about 0.1 A. The entire circuit is electronically

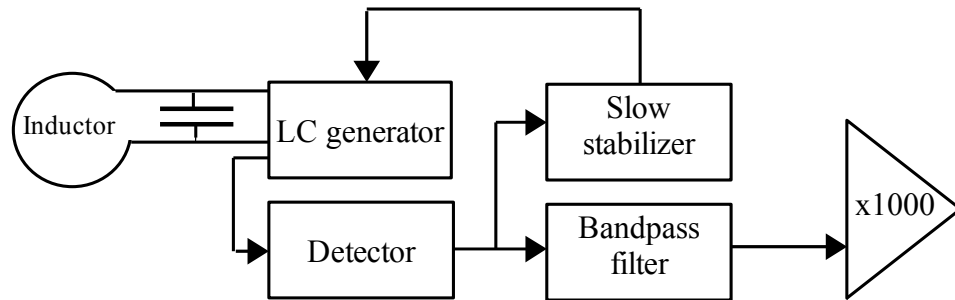


Fig. 1. Foucault cardiograph block diagram

shielded and put into a plastic enclosure being 160 mm × 160 mm × 60 mm in dimensions [7], [14]. Foucault device block diagram is shown in Fig.1. Detector stands for obtaining the signal, while bandpass filter sets allowed frequency band of sampled signal.

Sensitivity area of the Foucault sensor has a toroidal shape, which is coaxial with the inductor, thus the sensor it is completely insensitive in its axis of symmetry [5]. Inducted current density is inversely proportional to the distance from the inductor wire and depends on coil geometrical parameters (Fig.2). Sensitivity maximum lies on the inductor wire, thus signal recorded by the Foucault cardiograph is influenced more by the organs located closer to the coil than by further ones. According to the studies, signal obtained by the Foucault cardiograph depends on the sensor position on the patient's body. This dependence has been studied thoroughly [13].

Currently, the Foucault cardiography is under development. It has been shown that the technique is safe for conducting investigations on humans [14]. There is still a big deal of research required on the topic before making any conclusions about usage of the method. Secondly, question on how this device will be or can be used in practical purposes is unanswered. A lot of waveforms gathered from healthy patients have been recorded using the device, but studies of patients with heart conditions are also required.

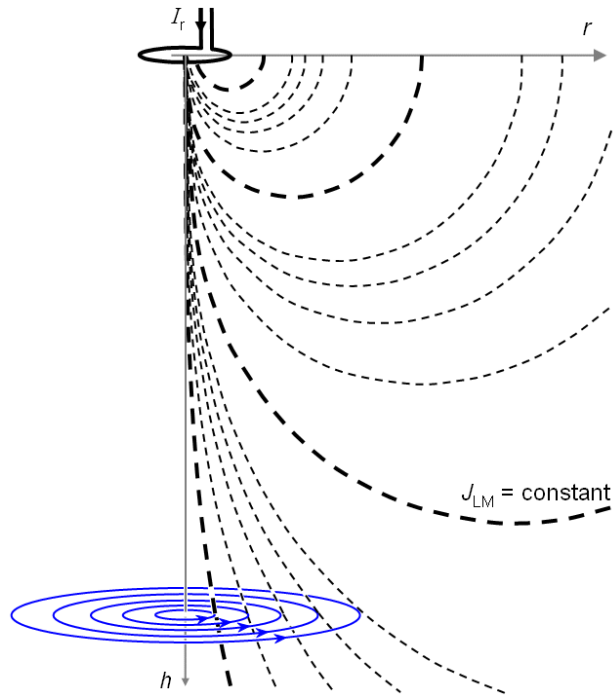


Fig. 2. Transducer sensitivity area. Dashed lines represent equipotential areas [5]

1.2 Foucault cardiogram waveforms

Foucault cardiogram output signal (FouCG) can be described as a quasi-periodical oscillation, which can be divided into cycles. Each one of these cycles characterizes physiological processes happening in the heart and thus provides an important clinical information. It can be seen in Fig.3 that FouCG curve reaches local maximum and minimum at the points of ventricular volume curve extremums.

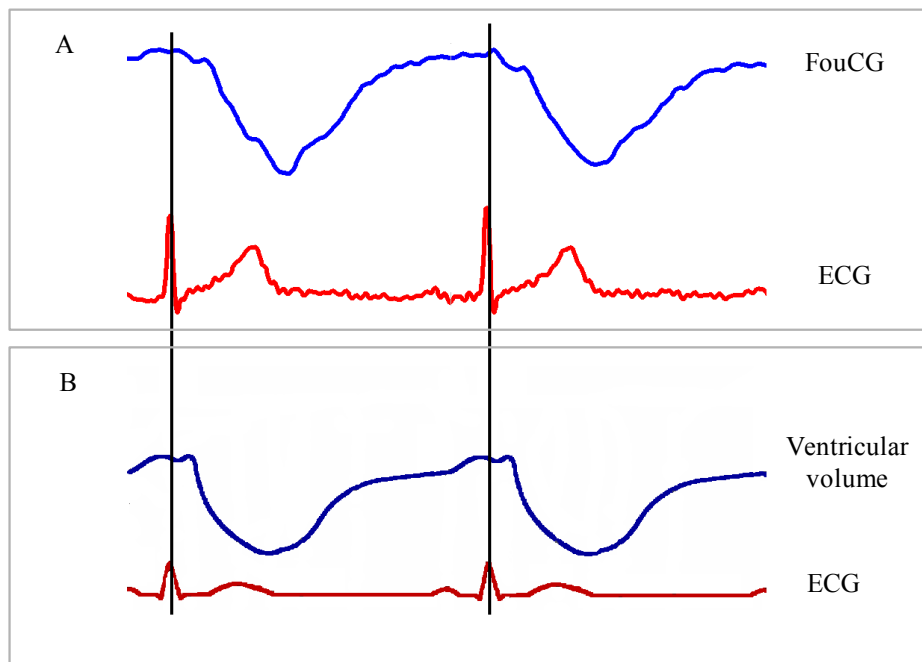


Fig. 3. Synchronically recorded ECG and FouCG signals (A). Ventricular volume curve and ECG recorded by Wiggers [3] (B)

Signal recorded from the thorax is influenced by physiological and physical processes. Cardiac and breathing originated components (Fig.4a) are considered to be main physiological parts of the signal. The cardiac originated component (Fig.4d) consists of two additive parts :

- the cardiac component itself, indicating changes in volume and shape of the heart during contraction;
- the arterial component, indicating pulsation of arterial blood vessels with the same rhythm as the heart contraction.

Breathing originated component (Fig.4c) consists of three additive parts [11]:

- the pulmonary component, which appears by changing of tissue conductivity during patient's breathing;
- the breathing originated component of cardiac origin, appearing because of heart movement relatively to the sensor due to diaphragm motion;
- the breathing originated component of volumetric cardiac origin, describing volumetric pulsation of mean blood volume in the heart as a result of physiological interaction of cardiac activity and breathing.

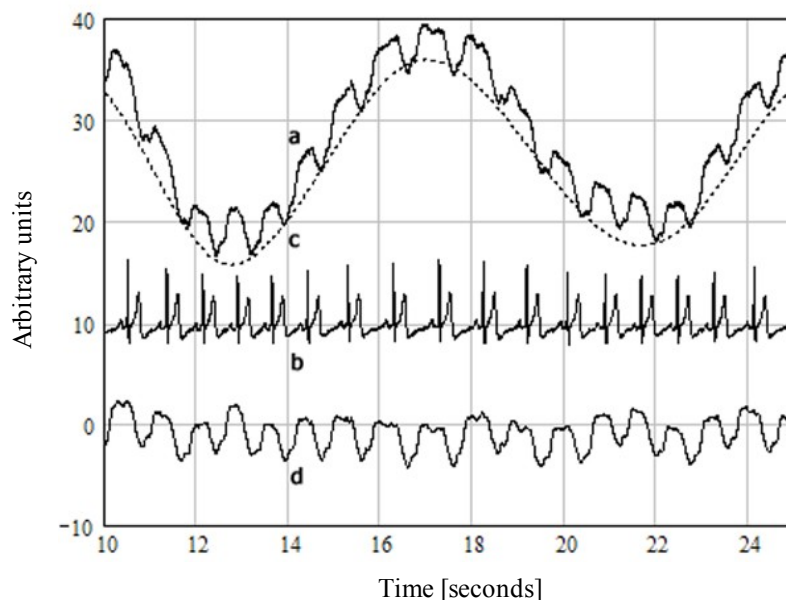


Fig. 4. Foucault cardiograph signal. a – unprocessed Foucault cardiograph output signal, b – ECG reading, c – breathing component, d – cardiac component

Main sources of interferences in the signal can be: *white noise* – statistically uncorrelated noise process with equal power distribution over frequency range,

existing in all electrical devices; *supply voltage noise* - appears when 50 Hz alternating current signal component and its harmonics are slipping into electrical circuits; *ADC (analog-to-digital converter) impulse noise* – as a strong deviation from current signal values due to conversion errors; *body movement artefacts* – based on sensor movement relative to the patient's body during investigation or any muscle contraction; *radio interference* – interference appearing due to electromagnetic radiation (by radio and TV stations, medical devices, unshielded computer cases, monitors, etc.). Since it is essential to track cardiac activity only, unwanted noises and the breathing component have to be removed from the signal. This problem has been resolved successfully in [10].

The exemplar of Foucault cardiograph built and still used at the University of Tartu cannot record and process signals simultaneously. To use any data in research, recorded as ASCII file raw signal is processed by appropriate mathematical algorithms.

One of such algorithms developed to process and display ensemble averaged waveform was written using MATLAB programming language [8]. Two signals, the FouCG and the synchronizing ECG, are recorded simultaneously and then filtered to remove noises.

An ensemble of the FouCG signal waves is formed by cutting the signal into pieces consisting of couples of adjacent signal cycles around the times of R-peak in the corresponding ECG. The pieces are aligned adhering their coincidence at R-peak points, and the mean value over the waves in the ensemble is calculated for each point of time, thus resulting in ensemble averaged waveform. Unfortunately, due to incoherence of natural heart activity, with the increase of temporal distance from the synchronizing ECG R-peak, the reliability of such raw waveform decreases. The reliability is the highest around the R-peak but falls independently to the left and to the right from this point. Therefore, the final waveform is combined from the left and right branches of the raw waveform using weighted average method. The inverse of the variance over all waves in the averaged ensemble, estimated for each time point, served as the weight.

Thus, a smooth resulting weighted ensemble averaged waveform is calculated. Currently this waveform is not calibrated against any units, but it is quite similar to the ventricular volume curve of the heart. Still there exists a great deal of uncertainty.

Thus it is necessary to compare FouCG waveform with reliable methods currently used in medicine for ventricular volume measurement.

1.3 Medical imaging techniques available for tracking cardiac activity

Modern medical imaging techniques are allowing physicians to monitor and study internal organs of the human body. As a result performance of typical clinical tasks can be done more safely and accurately. The following methods of medical imaging exist:

- Planar X-ray images - are projection images of a patient's region of interest. Those images are produced by the means of X-rays passing through body tissues and attenuated due to densities accordingly. X-ray method cannot be used for prolonged period of time due to hazardous X-ray radiation.
- Computed Tomography (CT) – technique based on the principle of conventional X-ray imaging with the difference, that stacks of axial slices are reconstructed mathematically to produce 3D images. X-ray based imaging is good for studying bone structure and fat tissue, but for acquisition of soft tissue images an invasive contrast agents have to be introduced. CT introduces even larger dose of X-ray radiation than convenient planar X-ray apparatus.
- Digital angiography - technique for producing images of patient's blood vessels. Contrast medium is used for producing images.
- Ultrasound imaging – based on usage of high frequency sound waves to produce images of internal structures by recording different reflecting signals. Ultrasound imaging is used for studying heart activity, with the one drawback that image quality produced is not of high-resolution compared to CT or MRI. Method is widely adopted because of being non-invasive, cost-effective and fast in acquisition.
- Positron Emission Tomography (PET) – is a functional imaging technique, which uses radioactive isotopes to localize pathological process by the means of gamma rays emission. Since radioactive isotope have to be introduced into patient's body this is invasive method and very cost-ineffective.

- Magnetic Resonance Imaging (MRI), based on absorption of energy from source at a particular resonant frequency. In MRI radio frequency pulses modify magnetization of hydrogen nuclei while being in external magnetic field. When hydrogen nuclei return to their initial state a radio frequency energy is being released. To reflect different structures of tissue different characteristics of the emitted magnetic resonance signal with different spatial localization are applied. MRI is non-invasive method providing high-resolution images, while usage of radio waves is much more safer than X-rays or radioactive isotopes. Drawback can be in its expensiveness and time frame required for one measurement.

It can be concluded that MRI imaging is rather convenient method for cardiac studies due to its safety for the patient and high-resolution output images.

1.4 Previous work done on determining heart ventricular volume with commonly used medical imaging techniques

MRI is a relatively new technology. The first image of living tissue was done in 1974, three years later first studies on humans were performed. MRI is used to distinguish healthy tissue from diseased one in medicine with advantage, that this is harmless technique. Technique used for studying the heart with MRI is called cardiac MRI. It continues to develop and advance. Cardiac MRI accurately depicts internal structure of the heart, its functionality, perfusion and myocardial viability with resolution and quality unmatched by other medical imaging techniques. MRI is widely accepted and used tool for cardiovascular research, since there has been considerable technical and clinical advancements over the last years such as improvements in temporal and spatial resolution, artefact reduction and contrast enhancement for perfusion analysis [24]. MRI is important diagnostic technique for cardiac studies and evaluation of various heart diseases [20].

J. L. Wang et al. [23] conducted research on determination of left ventricle volume using MRI. Ten axial slices of left ventricle being 8 *mm* in thickness and 1 *mm* in spatial resolution were produced using ECG gating. An algorithm for calculating ventricular volume of the heart was developed. Determination of endocaridal boundaries have been achieved with the semi-automatic procedure based on MATLAB grey level auto-contouring algorithm. A correction algorithm was

developed to adjust incorrectly detected contours, but it required a presence of an operator to assess quality of such procedure. The volume-time curve of the left ventricle was produced as result of research.

N. G. Bellenger et al. [25] compared most of medical imaging techniques currently in use for possibility of accurate determination of the left ventricle ejection fraction. M-mode 2D echocardiography was performed by experienced operators. Ejection fraction was evaluated with Simpson's biplane method of discs. Measurement of ejection fraction has been done using radionuclide ventriculography technique and cardiac MRI also. Produced images were processed mostly manually or using some proprietary software for image analysis. Authors showed that echocardiography technique is suitable enough for determination of heart ejection fraction, but result is influenced greatly by produced image quality. Simpson biplane 2D echo method is considered to be more accurate than M-mode method, but both of them extrapolate data from limited resolution image. As for studies with radionuclide ventriculography, they suffer greatly from poor resolution, while cardiac MRI is proven to be both accurate and of high image quality. And thus it was highly recommended as method for these types of studies.

Z. Zeidan et al. [16] studied real time 3D echocardiography on problem of production accurate volume-time curves of the heart ventricles. Volume-time curves calculated from cardiac MRI were used as reference. Both healthy and patients with heart pathologies were studied. Echocardiographic scanning was done by 2.5 MHz matrix-array transducer while the patient being in the left supine position. Recorded echocardiographic images were processed semi-automatically using proprietary software shipping with the device and volume-time curves calculated. Good agreement between 3D echo and MRI has been found which made 3D echocardiography well-suitable method for determining ejection fraction and volume-time curves of the heart ventricles.

M. García de Pablo et al. [17] worked on implementation of easy and convenient tool to segment the images obtained from cardiac MRI studies. A segmentation algorithm was based on the active contour models, but operator had to initialize the contour of the first image manually in order to start the segmentation. The images were processed iteratively and previous result of the segmentation was used as the initial contour for the following image. The problem of segmenting the papillary muscles correctly arose while the images were processed using the active

contours algorithm. Segmentation with the active contours was deemed suitable for MRI images segmentation process.

Bio-medical engineering (BME) group of the University of Tartu have conducted research on heart motion measurements using the MRI and FouCG techniques [9], [15]. An attempt has been made to explain difference in the FouCG signal measured at different body positions. Ventricular volume-time curves calculated from MRI images by simple threshold algorithm written in MATLAB have been compared with the FouCG signal obtained from different body positions. The algorithm had to be controlled manually to make it suitable for other data sets. Due to approach used, real volume units could not be derived when calculating ventricular volume curves. Since curves were very coarse and there has been problem in determination of exact heart cycle, interpretation of the results was difficult. Some similarities between two curves could be noted qualitatively, but comparison could not be conducted because MRI ventricle volume-time curve and FouCG signal were generally different and some additional information needed was absent.

F. Jamali Dinam et al. [22] provided an application for the new active contour algorithm based on Chan-Vese [29] approach. Since it is possible to detect the objects with smooth or discontinued boundaries using proposed model, contours both with and without gradients have been detected. The Algorithm has been extended to possibility of 3D surface detection and applied to detection of cardiac wall in the left ventricle. It has been shown, that method can track the cardiac motion in all three dimensions with significant resolution. Segmented results are turned out to be within small error compared to the manual segmentation.

S. Zambal et al. [28] developed heart segmentation algorithm on MRI images further. Initialization parameters such as orientation, position and model scale have been determined by the algorithm automatically. The circled Hough-transform was adapted to grey levels of images to perform detection of the left ventricle. This method has been applied to 42 MRI studies in total. Comparison between automatic segmentation and manual segmentation has been done with great success. As a result an automatic robust method for localization of left and right ventricles has been introduced. Some elementary image processing operators were used as well to increase quality of processed results. It has been shown that proposed method is of high performance and suitable for clinical application.

1.5 Statement of the problem

The Foucault cardiography method is entirely in prototype state, meaning it is not in use for clinical research to assess patient's health.

The objective of the present work is to compare the Foucault cardiogram with the ventricular volume-time curve obtained from cardiac MRI study in order to clarify the ability of the FouCG method to represent physiological processes of ventricular mechanical activity.

Based on problem review the solution of current problem is required for certain fields of medicine. To achieve the project goals successfully, the following tasks have to be fulfilled:

1. Plan and conduct cardiac MRI study on a human volunteer.
2. Record Foucault cardiogram from the same volunteer.
3. Develop appropriate digital image processing algorithm suitable for obtaining ventricular volume curves from cardiac MRI.
4. Implement digital image processing algorithm as MATLAB application.
5. Process FouCG signal to remove unwanted artefacts and obtain ensemble averaged waveform from it.
6. Compare ensemble averaged FouCG waveform with ventricular volume-time curve calculated by MRI image processing algorithm.
7. Analyse the results.

2 MATERIALS AND METHODS

2.1 Signa HDe 1.5T MRI system

Signa HDe 1.5T MRI, produced by GE medical systems is a high performance whole body MRI system featuring an actively shielded magnet, detachable patient table and phased array digital RF electronics. It utilizes the superconducting magnet operating at 1.5 *Tesla*. HDe data pipeline delivers imaging through 8 data channels linked to the Symmetric Vector Processor, that provides 850 2D fast Fourier transform operations per second for a matrix of 256×256 with simultaneous image reconstruction and acquisition. Multiple independent coils per channel can be used during acquisition. Images are reconstructed using 2D and 3D Fourier transformation techniques.

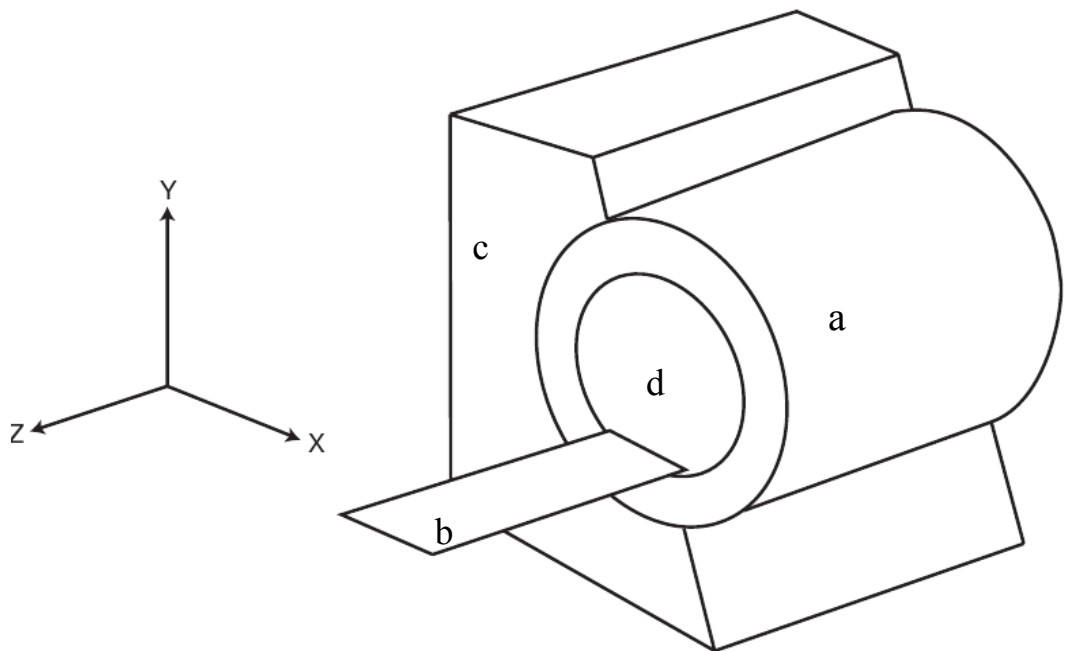


Fig. 5. MRI device schematic image. a – magnet assembly, b – patient table, c – control electronics, d – patient opening.

Device specifications are following:

- Width (Fig.5 along x-axis): 3.3 *m*, length (Fig.5 along z-axis): 6 *m*, height (Fig.5 along y-axis): 2.41 *m*
- Patient's opening diameter (Fig.5d): 0.6 *m*, toroid length (Fig.5a along z-axis): 1.72 *m*

- Power requirements: 8 *kVA* (standby), 18 *kVA* (average), 45 *kVA* (continuous sustained), 56.2 *kVA* (peak instantaneous).
- Magnet type: superconducting 1.5 *Tesla*
- Maximum image resolution: 256×256 pixels
- Surface coils: head, body, abdomen, spine, breast, knee, shoulder, cardiac imaging coils.
- Synchronization: ECG gating, respiratory gating
- Imaging modes: 2D single slice, multi slice, 3D volume images, multi slab, cine
- Field of view (FOV): 1 *cm* to 48 *cm* continuous
- Slice thickness: 2D 0.7 *mm* to 20 *mm*; 3D 0.1 *mm* to 5 *mm*
- Pixel intensity: 256 grey levels
- Cryogen use: less than 0.03 *L/hr* liquid helium

MRI device includes a detachable patient table (Fig.5b) with automated vertical and longitudinal power drives for easy patient positioning and safety. Laser guidance is used to assist in proper patient positioning along the device axis.

2.2 GE LOGIQ 3 ultrasound system

GE LOGIQ 3 ultrasound is an advanced ultrasound instrument which is used for broad range of clinical applications. It is portable and easy to use device. System parameters are:

- Width: 50 *cm*, length: 13.6 *cm*, height: 95.5 *cm*, weight: 153 *kg*
- Probe frequency: 1.5-3.6 *MHz*
- Modes: B-Mode, B/M-Mode, M-Mode, Anatomic M-Mode (AMM)

2.3 Foucault cardiography device

In the current study the Foucault cardiograph with a single-turn coil sensor is used (Fig.6). Apparatus consists of sensor (Fig.7), radio frequency generator, signal

detector, bandpass filter, signal amplifier, analog-to-digital converter (ADC) and a laptop PC for signal recording. Main parameters of the device are following:

- Sensor coil diameter: 135 mm, sensor current: 0.1 A, sensor voltage: 1.1 V
- Generator frequency: 7.7 MHz
- Maximum recording time: 120 s, signal sampling frequency: 250 Hz
- Intel 80486 SX33 Laptop PC with 2 MB RAM



Fig. 6. Foucault cardiograph device

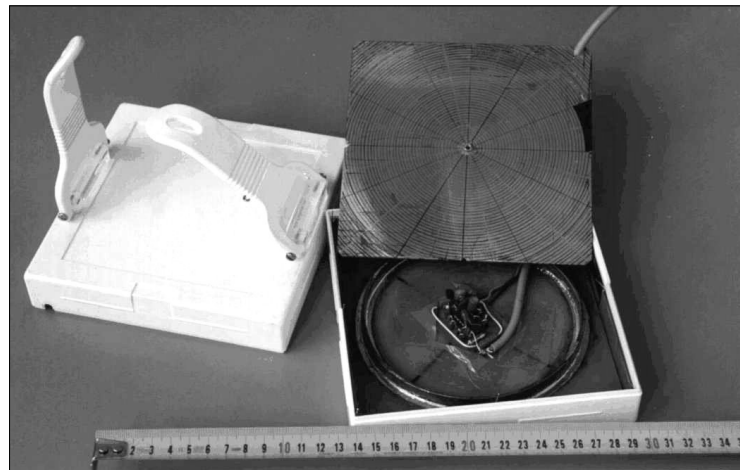


Fig. 7. Foucault cardiograph sensor

2.4 DICOM file format

DICOM (Digital Imaging and Communications in Medicine) [35] is a standard based on Open System Interconnection standard developed by NEMA (National Electrical Manufacturers Association) and supported by various producers of medical equipment. Format is used for creation, storage, transmission, printing and handling information in medical imaging. It consists of file format definition and

communication protocol. TCP/IP is used to communicate between medical devices in PACS (Picture Archiving and Communication System). DICOM groups information in the data-sets meaning incorporation of patient ID, study related information and image itself into one file. File format is an object oriented file with tag organization. Information model of DICOM consists of the following steps: patient →study→series→image. DICOM file descriptor tag consists of the following information:

- Patient attributes and demographic data
- Description of device model and produced company
- Medical institution attributes
- Researcher attributes
- Study type and date
- Study conditions and parameters
- Imaging series parameters
- DICOM unique identifier

Image data is compressed using various formats like JPEG, lossless JPEG, JPEG 2000, and Run-length encoding. DICOM integrates medical devices from various producers including DICOM scanners and DICOM servers and radiology stations into unified radiology information system. There are a lot of both proprietary and freeware software that allows to work with DICOM file format. In our work we use MATLAB programming language to process DICOM images.

2.5 Signal processing methods

When it comes to the processing the signal obtained during experiment, the common terms and techniques of signal processing will be used. A vast majority of measuring systems in physical experiments can be described in terms of *linear time invariant* (LTI) systems. Main property of last can be response to a sinusoidal input signal by a sinusoidal output signal different in amplitude and phase. LTI systems gained a considerable part of academic attention due to their predictability. Linearity and time-invariance are the most important properties of LTI systems.

Let $f(t)$ be a continuous-time input signal and $g(t)$ - continuous-time output signal, where t is a continuous variable, $f_\tau(t)=f(t-\tau)$ - shifted in time input signal, τ - time shift, L - LTI system operator. The output signal of LTI system is following: $g(t)=Lf(t)$.

The *impulse response* $h(t)$ of a continuous LTI is presented as response to the Dirac delta function $\delta(t)$:

$$h(t)=L\delta(t)$$

The input signal can be expressed as $f(t)=\int_{-\infty}^{\infty} f(\tau)\delta(t-\tau)d\tau$. Since the system is linear, the response of the system to an arbitrary input can be expressed as

$$g(t)=Lf(t)=L\int_{-\infty}^{\infty} f(\tau)\delta(t-\tau)d\tau=\int_{-\infty}^{\infty} f(\tau)L\delta(t-\tau)d\tau$$

By making substitution $h(t-\tau)=L\delta(t-\tau)$, we obtain LTI system characterized by its impulse response:

$$g(t)=\int_{-\infty}^{\infty} f(\tau)h(t-\tau)d\tau=f(t)*h(t) \quad (1)$$

Where $f(t)*h(t)$ is a convolution operation. The signal filtering (see Fig.8) is a procedure equivalent to the convolution of the input signal with the system impulse response. The filtered signal will be expressed as input signal convolved with appropriate filter impulse response: $g(t)=f(t)*h(t)$.

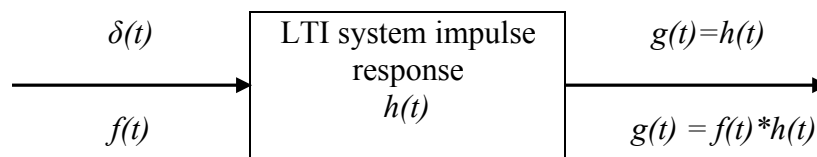


Fig. 8.LTI system

The equation (1) can be extended to the two dimensional signal:

$$g(x, y)=\int_{-\infty}^{\infty} \int_{-\infty}^{\infty} f(\xi, \gamma)h(x-\xi, y-\gamma)d\xi d\gamma=f(x, y)*h(x, y) \quad (2)$$

Let us define the Fourier transform as:

$$F(\omega)=\int_{-\infty}^{\infty} f(t)e^{-i\omega t}dt \quad (3)$$

where ω is an angular frequency of the signal. A function $f(t) \in L^2(\mathbb{R})$ is a square integrable function and thus represents itself as a processes with limited energy

values $\int_{-\infty}^{\infty} f(t) e^{-i\omega t} dt < \infty$. The Fourier transform of the function is a complex

function itself and can be generally expressed as $F(\omega) = |F(\omega)| e^{i\phi(\omega)}$. The quantities $|F(\omega)|$ and $e^{i\phi(\omega)}$ are called magnitude and phase spectrum of the function $f(t)$ respectively. If the function $F(\omega)$ is a square integrable function, an inverse Fourier transform can be defined also:

$$f(t) = \frac{1}{2\pi} \int_{-\infty}^{\infty} F(\omega) e^{i\omega t} d\omega \quad (4)$$

The convolution in time domain simplifies to the multiplication in frequency domain. If the output spectrum of the signal is $G(\omega)$, the input spectrum is $F(\omega)$, and $H(\omega)$ is the LTI system frequency response, then :

$$G(\omega) = F(\omega) H(\omega) \quad (5)$$

The equations (3),(4) and (5) can be extended to the two dimensional signal:

$$F(\xi, \gamma) = \int_{-\infty}^{\infty} \int_{-\infty}^{\infty} f(x, y) e^{-i\xi x} e^{-i\gamma y} dx dy \quad (6)$$

$$f(x, y) = \frac{1}{4\pi^2} \int_{-\infty}^{\infty} \int_{-\infty}^{\infty} F(\xi, \gamma) e^{i\xi x} e^{i\gamma y} d\xi d\gamma \quad (7)$$

$$G(\xi, \gamma) = F(\xi, \gamma) H(\xi, \gamma) \quad (8)$$

Since there are digitally sampled signals used in computational software, their filtering done similarly to the equations (6-8). The Fourier transform pairs (6), (7) for a discrete signal of size X by Y become:

$$F(p, q) = \sum_{x=0}^{X-1} \sum_{y=0}^{Y-1} f(x, y) e^{-i(2\pi/X)px} e^{-i(2\pi/Y)qy} \quad (9),$$

where $p=0, 1.. X-1$ and $q=0, 1.. Y-1$

The values $F(p, q)$ are the Fourier transform coefficients of $f(x, y)$. The discrete form of inverse Fourier transform becomes:

$$f(x, y) = \frac{1}{XY} \sum_{p=0}^{X-1} \sum_{q=0}^{Y-1} F(p, q) e^{i(2\pi/X)px} e^{i(2\pi/Y)qy} \quad (10),$$

where $x=0,1..X-1$ and $y=0,1..Y-1$

Both the Fourier and inverse Fourier transform computations are supported by MATLAB functions. The two dimensional Fourier transform is calculated by $F = \text{fft2}(f, X, Y)$ operation, where F is an output matrix and f is an input matrix, the two dimensional inverse Fourier transform is calculated by $f = \text{ifft2}(F, X, Y)$.

MATLAB computes Fourier transforms using a fast Fourier transform algorithms. To compute an N - point discrete Fourier transform when $N = N_1 N_2$ is composite, the *fft* library decomposes the problem using the Cooley-Tukey algorithm, which first computes N_1 transforms of size N_2 , and then computes N_2 transforms of size N_1 . The decomposition is applied recursively to both the N_1 - and N_2 - point discrete Fourier transforms until the problem can be solved using one of several machine-generated fixed-size "codelets.". The codelets in turn use several algorithms in combination, including a variation of Cooley-Tukey, a prime factor algorithm, and a split-radix algorithm. The particular factorization of N is chosen heuristically.

When N is a prime number, the *fft* function first decomposes an N - point problem into three $(N-1)$ - point problems using Rader's algorithm. It then uses the Cooley-Tukey decomposition to compute the $(N-1)$ - point transforms.

For most N , real-input discrete Fourier transforms require roughly half the computation time of complex-input Fourier transforms. However, when N has large prime factors, there is little or no speed difference.

The execution time for *fft* depends on the length of the transform. It is fastest for powers of two. It is almost as fast for lengths that have only small prime factors. It is typically several times slower for prime lengths or which have large prime factors.

As we have shown in (5) continuous- or discrete-time LTI system acts as a filter on the input signal. The filter is a system that exhibits the frequency-selective behavior, when it is necessary to suppress some unwanted frequency components. There four main types of ideal digital filters exist: *low-pass*, *high-pass*, *band-pass* and *band-stop* filter. In discrete-time systems it is necessary to obey the *Nyquist sampling theorem*, which states that sampled analog signal does not suffer from aliasing effects when sampling frequency is two times higher of the maximum signal frequency. Digital filters are described using amplitude-frequency response $|H(\omega)|$. Let us

show an amplitude-frequency response of common ideal filters. The low-pass filter (Fig.9a) is specified by:

$$|H(\omega)|=1 \text{ if } |\omega|<\omega_c, 0 \text{ if } |\omega|>\omega_c \quad (11)$$

The high-pass (Fig.9b) filter is specified by:

$$|H(\omega)|=0 \text{ if } |\omega|<\omega_c, 1 \text{ if } |\omega|>\omega_c \quad (12)$$

The band-pass (Fig.9c) filter is specified by:

$$|H(\omega)|=1 \text{ if } \omega_1<|\omega|<\omega_2, 0 \text{ otherwise} \quad (13)$$

The band-stop (Fig.9d) filter is specified by:

$$|H(\omega)|=0 \text{ if } \omega_1<|\omega|<\omega_2, 1 \text{ otherwise} \quad (14)$$

Where ω_c is cutoff frequency.

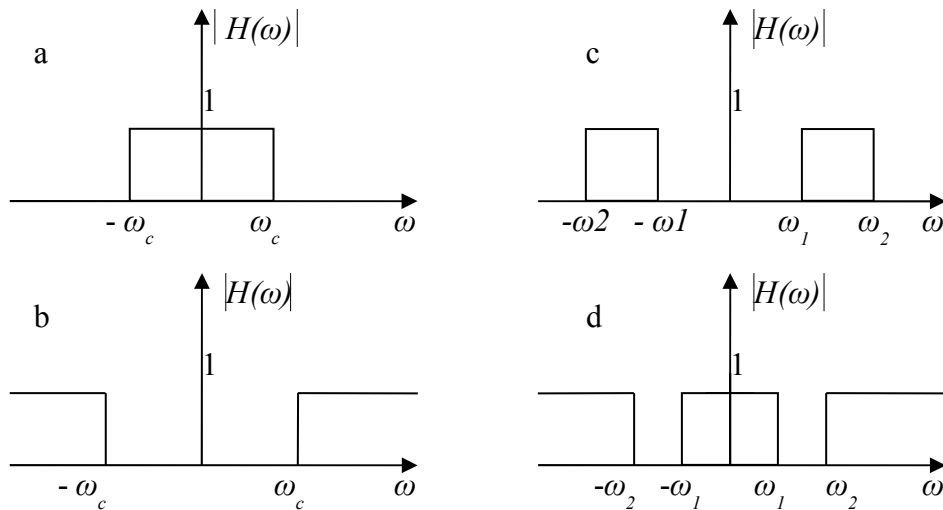


Fig. 9. Amplitude-frequency response of ideal digital filters.

LTI system principles as well as digital filtering will be used for processing the FouCG signal as well as filtering MRI images.

2.6 Digital image processing methods

A digital image is a two-dimensional signal of a form $f(x, y)$. The values of a function f at spatial coordinates (x, y) are positive scalars, whose physical meaning determined by the image source (MRI scan). Generally the pixel values of digital images lie in the following boundaries:

$$0 \leq f(x, y) \leq 255$$

Common image enhancement techniques fall into spatial domain or direct manipulation of image pixels. Spatial domain processes can be described by equation:

$$g(x, y) = Tf(x, y) \quad (15)$$

where $f(x, y)$ is an input image, $g(x, y)$ is an output (processed) image, T is an operator. When the size of operator T is one pixel it becomes the grey-level transformation function.

Function *imadjust* is used for intensity transformations of grey-scale images in MATLAB. Its syntax is following: $g = \text{imadjust}(f)$ (16). This function can be used to archive appropriate contrast of desired image region. Another method of contrast adjustment in digital images called histogram equalization. It is implemented as $g = \text{histeq}(f)$ (17a).

There is often necessity to remove noise from images to improve results of latter processing. Median filtering is the most suitable method for such task. It is a nonlinear operation used to reduce "salt and pepper" noise on images. A median filtering is more effective method than convolution because it preserves edges and removes high-frequency noises as well. It is implemented as $g = \text{medfilt2}(f)$ (17b).

Kernel image filtering is based on two-dimensional convolution (2). Sobel edge detecting and smooth/sharp 3×3 kernels used in this work are shown below:

$$h_{\text{Sobel-x}} = \begin{vmatrix} -1 & -2 & -1 \\ 0 & 0 & 0 \\ 1 & 2 & 1 \end{vmatrix} \quad h_{\text{Sobel-y}} = \begin{vmatrix} 1 & 0 & -1 \\ 2 & 0 & 2 \\ 1 & 0 & 1 \end{vmatrix} \quad (18)$$

$$h_{\text{smooth}} = \frac{1}{16} \begin{vmatrix} 1 & 2 & 1 \\ 2 & 4 & 2 \\ 1 & 2 & 1 \end{vmatrix} \quad h_{\text{sharp}} = \begin{vmatrix} -1 & -1 & -1 \\ -1 & 9 & -1 \\ -1 & -1 & -1 \end{vmatrix} \quad (19)$$

Frequency domain processing of digital images is based on two-dimensional fast Fourier transform techniques, described by equations (9-10) and application of digital filters (8). Schematically the process is shown in (Fig.10).

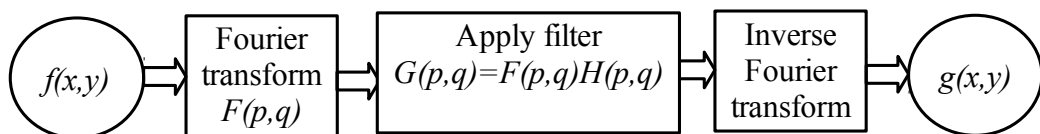


Fig. 10. Image filtering process with two-dimensional FFT

Four types of digital filters, described by equations (11-14) and transformed to two-dimensional form can be used as $H(p, q)$.

2.7 Active contours as method for image segmentation

An active contour [30], [31], [32] is an energy-minimizing spline guided by external constraint forces and influenced by image forces that pull it towards image features such as lines or edges. Basic idea of the active contours is to evolve a curve, subject to constraints from a given image in order to detect desired objects. Active contours lock onto nearby edges accurately during iterative computational process.

Let us represent position of an active contour parametrically $c(s)=(x(s), y(s))$ and write its energy functional as

$$E_{contour} = \int_0^1 E_{internal}(c(s)) + E_{image}(c(s)) + E_{con}(c(s)) ds \quad (20)$$

Where $E_{internal}$ represent the internal energy of spline due to bending, E_{image} gives rise to the image forces and E_{con} gives rise to the external constraint forces.

The internal energy spline can be written as

$$E_{internal} = \frac{1}{2} (\alpha(s) |c_s(s)|^2 + \beta(s) |c_{ss}(s)|^2) \quad (21)$$

The spline energy consists of a first-order term controlled by $\alpha(s)$ and a second order term controlled by $\beta(s)$. The first-order term makes contour act like a membrane and the second-order term makes it act like a thin plate. Setting $\beta(s)$ to zero allows contour to become second-order and develop a corner. Contour minimization procedure is iterative technique. Each iteration takes implicit Euler steps with respect to the internal energy and explicit Euler steps with respect to the image and external constraint energy.

In order to apply active contours to the image, energy functionals that attracted to desired features of images are required. These features can be lines, edges and terminators. Total image energy can be expressed as a weighted combination of three energy functionals:

$$E_{image} = \alpha E_{line} + \beta E_{edge} + \gamma E_{term} \quad (22).$$

Weight adjustment specifies what features of the digital image influence the active contour at most.

The simplest image feature is intensity itself. If we define

$$E_{line} = I(x, y) \quad (23),$$

then depending on α sign contour will be attracted either to dark or light lines of the image.

Detection of edges in images can be done with simple energy functional. By using equations (2) and (18) we obtain:

$$E_{edge} = I(x, y) * h_{Sobel-x} + I(x, y) * h_{Sobel-y} \quad (24).$$

The active contour gets attracted to the features containing edges.

In order to find terminators of line segments and corners, curvature of level lines in a slightly smoothed image used. Applying kernel (19) to the image we will obtain its smoothed version $G(x, y) = I(x, y) * h_{smooth}(x, y)$. Let

$\theta = \arctan\left(\frac{G_y}{G_x}\right)$ be the gradient angle, $n_{along} = (\cos(\theta), \sin(\theta))$ and $n_{perpendicular} = (-\sin(\theta), \cos(\theta))$ be unit vectors along and perpendicular to gradient direction respectively. Curvature of the level contours in $G(x, y)$ can be written

$$E_{term} = \frac{d\theta}{dn_{perpendicular}} = \frac{d^2 G(x, y) / dn_{perpendicular}^2}{dG(x, y) / dn_{along}} \quad (25).$$

By combining E_{edge} and E_{term} we can create active contour that is attracted to edges or terminators.

MATLAB implementation of active contours has been written for the purpose of segmentation of digital images obtained in cardiac MRI study.

2.8 Splines for curve fitting

To draw a smoothed curve based on sampled points, it is necessary to use interpolation methods to calculate curve values in between those points. Linear interpolation does not serve very well for plotting biological signals properly. Splines produce very smooth curves and describe biological signals more accurately. Splines are special functions defined by polynomials and used for the interpolation problems in current work. Cubic spline computation is implemented in MATLAB by

$$y_{interpolated} = spline(x, y) \quad (26) \text{ function. Since number of values in y-domain grows}$$

because of interpolation, number of values in x-domain gets “stretched” respectively by function $x_{stretched} = linspace(x, y_{interpolated})$ (27)

2.9 Similarity index between waveforms

Similarity index [8] combines several partial indices comprising the squares of following correlation coefficients:

- between the two compared waveforms themselves r_0 ,
- between their first derivatives r_1 ,
- between their second derivatives r_2 .

Similarity index R depends on the appropriate correlation coefficients in the following way:

$$R = [\alpha r_0^2 + (1 - \alpha)][\beta r_1^2 + (1 - \beta)][\gamma r_2^2 + (1 - \gamma)] ,$$

where α , β and γ stand for weights. We have chosen weights to be $\alpha \approx 0.58$, $\beta \approx 0.33$, $\gamma \approx 0.19$ in our work. The R value varies between 0 and 1 , and increases with the growth of similarity between compared waveforms.

3 DESCRIPTION OF WORK DONE

3.1 MRI research planning and conduction conditions

Based on statement of the problem it is necessary to set-up and conduct the cardiac MRI study on human's heart. It has to be conducted in such way, that possibility to obtain the ventricular volume-time curve existed. Cardiac cine MRI was performed on a healthy male volunteer (26 years old, height 185 cm, weight 94 kg) with 1.5 tesla Signa HDe at West Tallinn Central Hospital. The FouCG measurement have to be conducted on the same volunteer later, while trying to preserve his physical condition similar to one during MRI study.

During the first phase of MRI study we briefed the volunteer and started his preparation. Since breathing adds some artefacts to the output images during cardiac MRI procedure, it was explained that it would be necessary to hold one's breath for some time during image obtaining process. All metallic objects have been removed. They pose a great threat both to patient's life and MRI device itself, since in strong magnetic field metallic objects do accelerate.

During the second phase of preparation for the MRI, we placed the patient on the special positioning table of MRI apparatus. During this procedure we had to be sure that the patient feels himself as much as possible comfortable, since it takes approximately 30 minutes to properly conduct one MRI study. ECG electrodes had to be connected properly in order to obtain the ECG signal. The ECG signal is required during cardiac MRIs in order to implement ECG gating. The cardiac cycle is divided into equal time segments Δt and then MRI device takes one frame per each cycle, shifts time to another Δt for next image, thus obtaining frames, corresponding to the whole cardiac cycle. Process is illustrated schematically on (Fig.11).

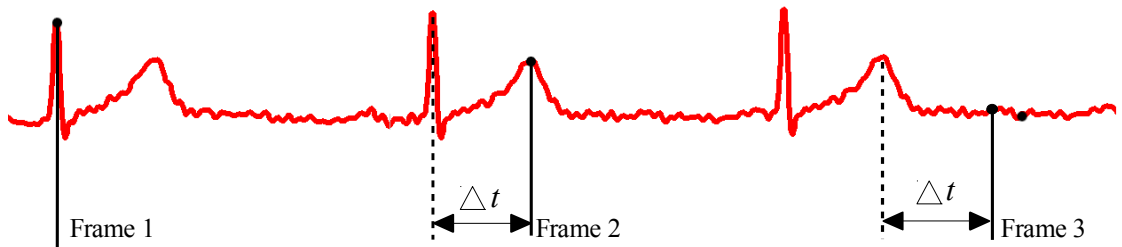


Fig. 11. Schematic representation of ECG gating during MRI research.

In our study cardiac cycle was divided into 20 equal segments with $\Delta t = 44 \text{ ms}$, giving us 20 frames per cardiac cycle.

When ECG electrodes and breathing belt sensor were finally in place, we have positioned cardiac surface coil on thoracic area effectively covering the heart of the patient (Fig.12).



Fig. 12. Patient prepared for MRI study. Large surface amplifier coil is on top.

Surface coil is used to amplify signal, thus making images obtained homogeneous in terms of intensity. Also surface coil helps to obtain output images with better resolution and lower signal-to-noise ratio. An emergency “panic button” has been given to the patient in case he feels himself uncomfortable inside MRI tube so he could give us a signal for his emergency removal.

Now the table's vertical axis have to be adjusted in order to make it equal to MRI axis. Special laser guided levels were used to set vertical and horizontal position to zero. To initialize the region of measurement interest, zero point of z axis has been placed right over the heart. The surface coil have markings on it showing common location of the heart in humans. With the help of laser guided levels, we have completed positioning of all three axis of the patient's table and prepared the MRI device to take a pictures of required region of our interest.

During the time of image obtaining process patient had to hold his breath for 15 seconds in order to reduce imaging artefacts related to body movement. Cardiac MRI study usually starts from a *scout image* of thoracic area. The scout is a very coarse image obtained, showing internal organ structure at low resolution. Five sagittal, coronal and axial scouts were produced (see Fig.13). The heart has been detected on scout images manually by the human operator. An imaging plane has been set on central scout slice so that *vertical long axis* of the heart could be obtained.

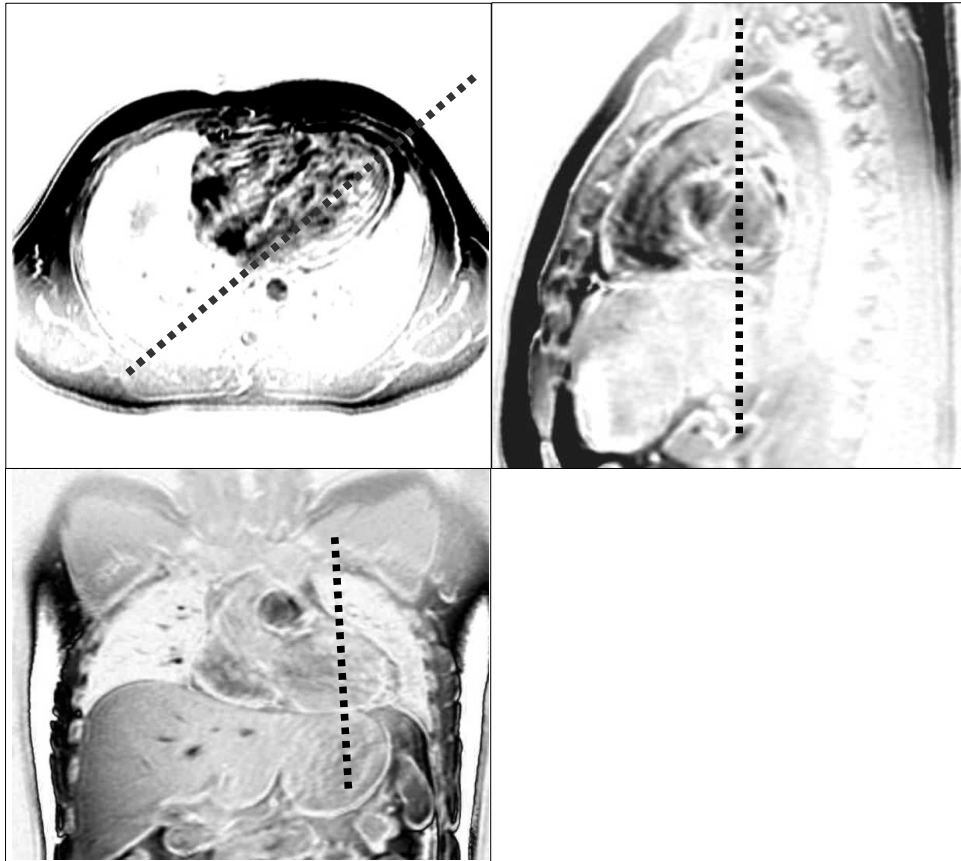


Fig. 13. Scout images in axial (top left), sagittal (top right) and coronal (bottom) planes relative to human body.

Imaging planes are shown by dashed line in every slicing place. Frames in vertical long axis of the heart were obtained using the scout image planes, thus giving us sagittal projection of the heart with respect to its position (see Fig. 14 left).

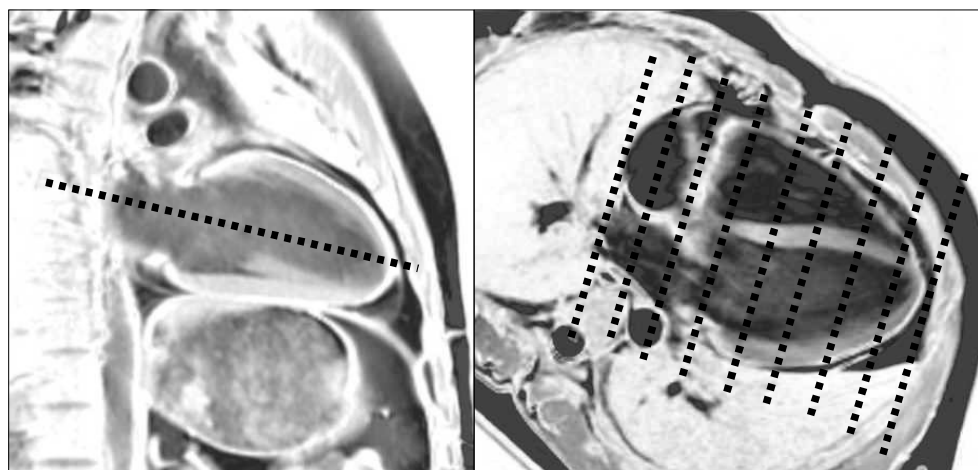


Fig. 14. Vertical long axis of the heart (left). Horizontal long axis of the heart (right)

Placing imaging plane as showed in (Fig. 14 left) will give us *horizontal long axis* of the heart (Fig. 14 right) or coronal projection of the heart with respect to its position. Cardiac wall may be observed on this projection, making shapes of the left and right

ventricles easily distinguishable. The most important for our study *short axis* projection of the heart or axial projection with respect to its position, can be obtained by placing image planes onto horizontal long axis projection. As illustrated in (Fig. 14 right) we have covered whole area of the heart from base to apex with imaging planes. We tried to place imaging planes as much as possible perpendicularly to the cardiac wall. Number of imaging planes was set to 18, which means that 18 slices in short axis projection each containing 20 frames in each slice would be obtained. As a result it gave us 360 DICOM images in total for processing. This is the longest part of the MRI study since sufficient time had to be given to the patient between measurement cycles for breath restoration. Obtained short axis images of the heart are illustrated in (Fig.15).

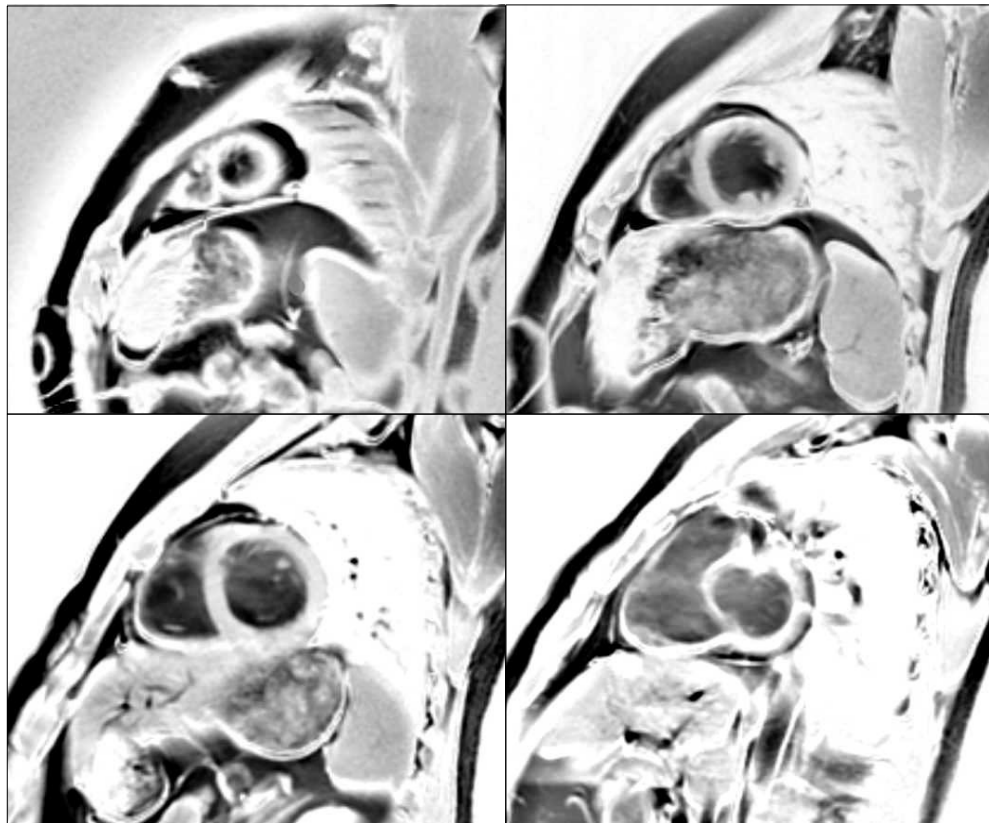


Fig. 15. Images from short axis of the heart: 2nd slice (top left), 6th slice (top right), 8th slice (bottom left), 10th slice (bottom right)

The whole MRI study procedure took us approximately 1 hour and 20 minutes to complete, which is two times longer than standard cardiac study normally conducted at the hospital. Reason for this lies in extension of measurement protocol in order to produce some additional images required for the scope of present thesis.

3.2 Ultrasound measurement of cardiac ejection fraction

Ultrasound measurement has been performed by an experienced operator on GE LOGIQ 3 ultrasound system 10 minutes after MRI procedures. The patient has been placed in a supine position and an echo transducer was placed over the heart region, while he rested. Transducer's position has been fine tuned in such way, that the both heart ventricles were displayed on the monitor simultaneously. We have recorded a couple of cardiac cycles after measurement hardware has been positioned properly. Ejection fraction was determined afterwards using build-in software to manually segment both left- and right ventricle at the systole and diastole (Fig.16)

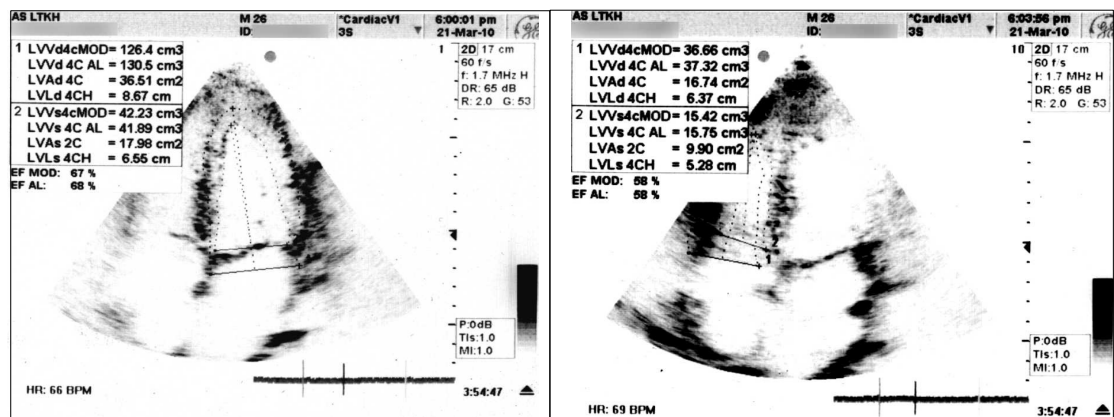


Fig. 16. Obtaining ejection fraction of left and right ventricles during ultrasound examination.

Simpson's biplane method of discs is used to approximate end-systolic (ESV) and end-diastolic volumes (EDV) of the ventricle. Ejection fraction (EF) has been calculated and turned to be equal to 67% and 58% for the left and right ventricle respectively. It took us about 5 minutes including appropriate calculations to conduct ultrasound measurement of ejection fraction, being a fastest measurement in the whole study.

3.3 Foucault cardiogram recording

Approximately 10 minutes after ultrasound measurements we started to conduct FouCG recording. We tried to preserve patient's position and state equal to the previous two experiments. Patient's condition could be described as stable and rest, breathing normal, heart rate 68 beats per minute. ECG electrodes were connected according to Einthoven II lead in order to record ECG signal simultaneously with FouCG. Central point of the Foucault inductor has been positioned slightly below the appropriate point on thoracic region known as the apex-beat. Such position allows to

obtain FouCG signal very similar to ventricular volume curve [12], [13]. In order to place inductor correctly following operations have to be completed (Fig. 17):

- Determine the position of the heart and its geometry inside human body using previously conducted MRI study.
- Find the apex-beat point of the heart (on the left side of rib-cage, approximately 2nd rib from below) on coronal MRI image of the body.
- Make two finger intent below the point placed in previous step. Marked as “X”.

By completing above steps the FouCG inductor coil should be on top of the ventricles. Other organs lying in the proximity of the coil should not influence the signal much.

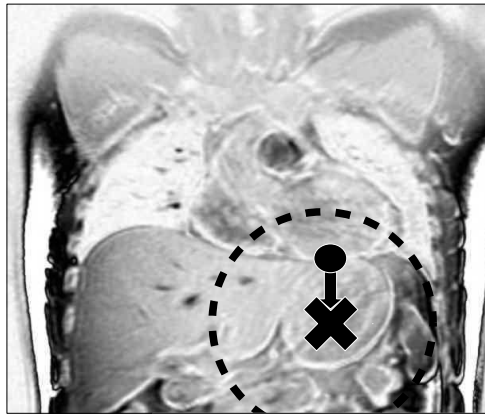


Fig. 17. Position of the Foucault inductor.

Raw FouCG and simultaneous ECG signals have been recorded for 2 minutes.

3.4 Image processing algorithm

During MRI study we have obtained a set of DICOM images. These images describe object under study in width and height if we take one image; width, height and time if we take image set of one slice; width, height, time and length if we take all slices into account. This makes our images 4-dimensional (4D). Let us define a 4D image function: $I = f(x, y, s, t)$, where $x = 1, 2 \dots X$; $y = 1, 2 \dots Y$ are the image coordinates, $s = 1, 2 \dots S$ is the spatial slice location and $t = 1, 2 \dots T$ is the temporal slice location. I_s^t will define a single image at spatial location s and time t .

During the first stage of image processing, DICOM images have been loaded into MATLAB for their pre-processing. A function called *preprocessing.m* (Appendix

9.1) has been programmed for this purpose. Schematically its flow is illustrated in (Fig. 18).

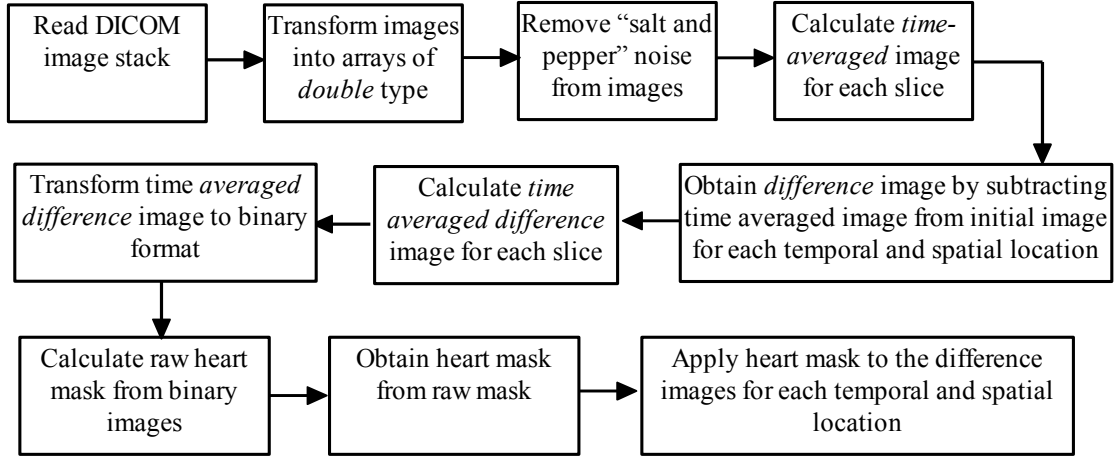


Fig. 18. Preprocessing algorithm flow

After 4D image stack is loaded and converted to double type arrays each pixel intensity becomes $f \in \mathcal{R} = [0,1]$. “Salt and pepper” noise gets removed by using median filter (Eq. 17b) with 3×3 kernel. The localization of the heart was done as proposed by Soegel et al. [18]. *Time-averaged* images for each slice is computed as

$$\bar{I}_s = \frac{1}{T} \sum_{t=1}^T I_s^t \quad (28)$$

and implemented as *mean_image_array* function. Then for each spatial location s *variance image* is computed as squared subtraction of time-averaged image from initial image at each spatial location $s=1,2..S$ and each temporal location $t=1,2..T$

$$D_s = \frac{1}{T} \sum_{t=1}^T (I_s^t - \bar{I}_s)^2 \quad (29)$$

This is implemented as *variance_image_array* function. Examples of variance images for different slice locations are illustrated in (Fig. 19). Position and orientation of the heart can be well seen on variance images. It should be noted that image pixel values obtained are high within contours of the heart, while outside of contours generally lower pixel values are found. As an explanation, this could be connected with very heavy blood flow inside the heart ventricles during cardiac cycle. The heart is well separated from the surrounding bone tissue and other organs inside the chest in variance images compared to original images (Fig. 15). However some objects not

related to the heart are still present on variance images computed. These objects are generated by the blood flow in other organs and vessels around them.

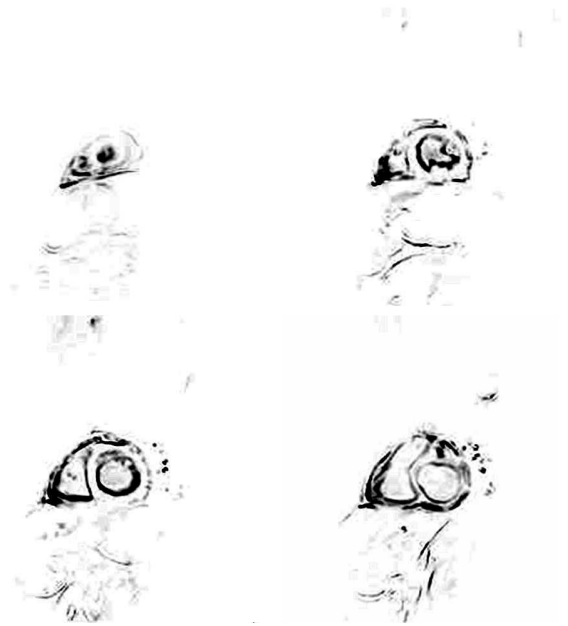


Fig. 19. Variance images computed at 2nd (top left), 6th (top right), 8th (bottom left) and 10th (bottom right) slice locations.

We have thresholded and transformed variance images to binary image format then. A contrast adjustment function (Eq. 16) have been applied to thresholded images [21]. A global threshold level for the image was computed using Otsu's method, which chooses the threshold according to minimization of the intraclass variance of the black and white pixels [27]. Image was converted to binary format using MATLAB function *im2bw*, which used contrast adjusted image and grey-level threshold as input. To remove some small artefacts not related to the heart region *bwareaopen* function has been used. Parameter of 50 pixels was chosen, meaning if some remote object on the image had an area less than 50 pixels it was deemed as artefact and thus removed. Generally thresholding is computed by applying appropriate image transform operator T_s , which describes algorithm used :

$$T_s = \Gamma(D_s) \quad (30)$$

Algorithm has been implemented as *binarize* function in MATLAB. Results of thresholding technique used are illustrated in (Fig.20). Some artefacts are present in

T_s images. Objects shown by dashed line were more than 50 pixels in area and passed through the soft filtering filtering function. Greater filtering area value was not chosen due to possibility of filtering pixels belonging to the heart area and loosing

some information as result. Another algorithm has been implemented to remove artefacts on variance images.

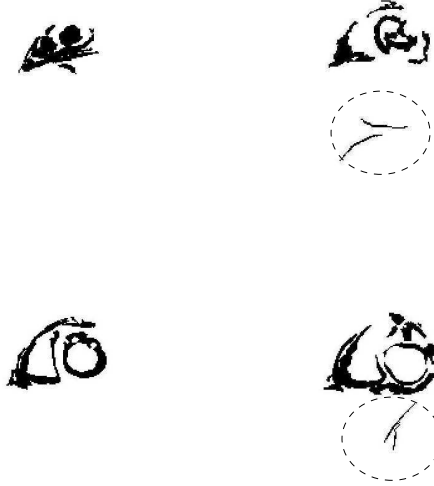


Fig. 20. Thresholded variance images at 2nd (top left), 6th (top right), 8th (bottom left) and 10th (bottom right) slice locations. Artefacts shown by dashed line.

Taking into account the fact, that pixel values on most variance images D_s the are belonging to the heart region more than other organs and its thresholded variant T_s appears to have similar behaviour, artefacts can be removed by using the appropriate heart mask. The raw heart mask can be computed as:

$$M = \frac{1}{S} \sum_{s=1}^S T_s \quad (31)$$

and illustrated in (Fig. 21)

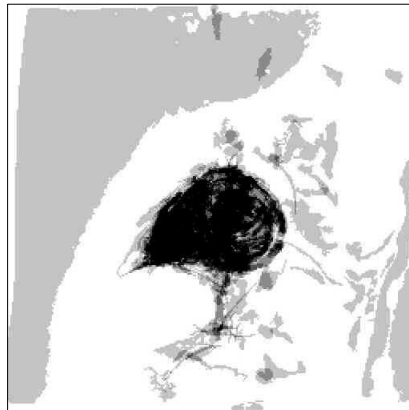


Fig. 21. Raw heart mask

Sub-function *vmi_mask* has been written for this purpose in MATLAB. Note, that pixel intensity on the raw mask corresponds to the existence probability of some particular object on T_s images, meaning if pixel intensity is at maximum this object

exists in all images, if pixel intensity is minimum it only exists in one image. Raw heart mask is thresholded according to (Eq. 30): $M_{thresholded} = \Gamma(M)$, with the only difference being in parameter of remove artefacts function *bwareaopen*. Now we could apply a 100 pixel filtering parameter due to the fact, that raw heart mask does not contain remote pixels in the heart region, meaning that they are all connected. Remote pixels and objects describe some other organs and blood vessels mostly, so they can be removed freely from the final mask. Sub-function *binarize_vmi_mask* has been implemented for this purpose. In case two or more relatively large objects obtained, heart is detected by selecting object containing greater pixel count. Algorithm is implemented by *find_heart* function. Results of the raw heart mask thresholding is illustrated in (Fig. 22)



Fig. 22. Cleaned heart mask

In the final step of the pre-processing algorithm the cleaned heart mask has been applied to thresholded variance images: $T_{cl} = M_{thresholded} T_s$. This process effectively removes unwanted artefacts. MATLAB function *applymask* has been developed for this purpose. Cleaned thresholded variance images are illustrated in (Fig. 23).



Fig. 23. Cleaned thresholded variance images at 6th (left), 10th (right) slice locations.

Segmentation of DICOM images with active contours, using cleaned thresholded variance images T_{cl} as initial contour would be the next stage of image processing. Algorithm flow is depicted in (Fig. 24) schematically.

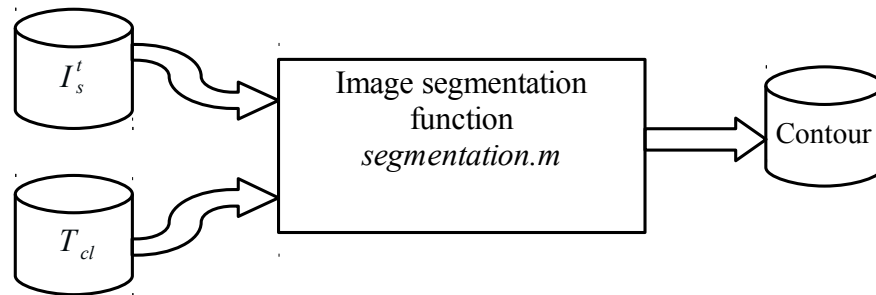


Fig. 24. Segmentation principle flow

Segmentation idea is based on the active contour principles, described by equations (20-22). Numerical computation algorithm has been programmed in MATLAB environment using Chan-Vese research paper [29] and MATLAB implementation of “snakes” [19]. Initially the algorithm allowed to segment 2D images only, so we had to extend it to work in 4D space also. Image segmentation algorithm *segmentation.m* (Appendix 9.1) has been realized in the following way:

1. Program checks if the proper variables like image to be segmented I_s^t , initial contour T_{cl} , boundary intensity value and number of iterations have been supplied.
2. Image I_s^t and T_{cl} are displayed on the screen to show initial conditions.
3. Main computation loop is initialized. It calculates constants c_1 and c_2 which are the averages of input image inside contour and outside contour respectively.
4. Based on constants c_1 and c_2 it is decided should contour grow larger over object or shrink further.
5. Intermediate contour is displayed over initial image I_s^t to visualize behaviour.
6. Iteration stop condition is controlled. If previous and current contour difference is a very small value, computation iterations stops to save time.
7. Final contour value C is shown on screen and saved as appropriate variable.

After segmentation a coarse contours of the heart region have been obtained (Fig.25).

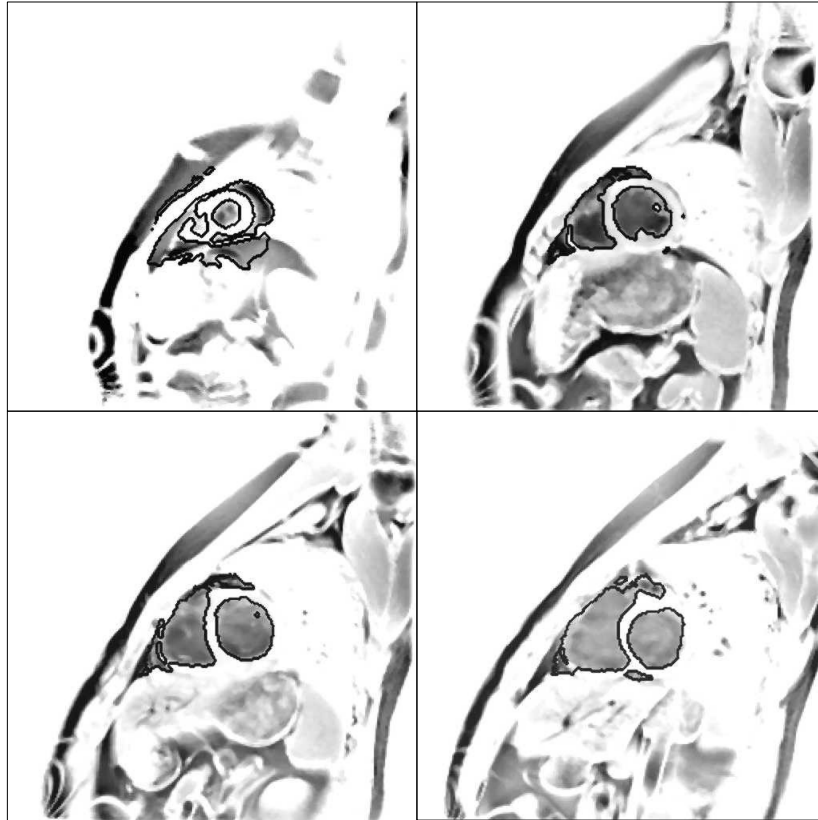


Fig. 25. Heart short axis MRI images with coarse ventricular contours at 2nd (top left), 6th (top right), 8th (bottom left) and 10th (bottom right) slice locations

It is noticeable, that contours obtained describe not only left and right ventricles, but also some muscle and fat tissues, which have been detected due to their high pixel intensity. Some countermeasures had to be implemented to obtain only left and right ventricle contours.

The algorithm *post_segment_processing.m* (Appendix 9.1) has been developed for finding ventricles and cleaning contours. Contour images are taken as input for further processing. Schematically program steps are plotted in (Fig.26)

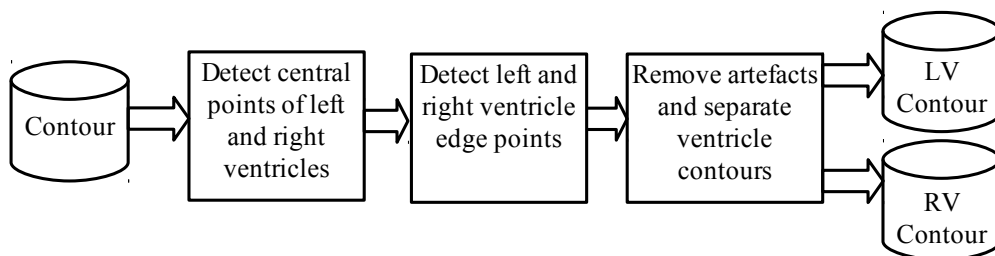


Fig. 26. Post segmentation processing algorithm flow.

Each step of the algorithm is logically and programmatically complex MATLAB sub-function. To detect central point of the both left and right ventricle following algorithm has been implemented (Fig.27):

1. Temporal mean contour C_{mean} is obtained for each slice from C using (Eq. 28).
2. Contour with filled holes and gaps C_{nh} is calculated from C_{mean} for each slice using *close_holes_on_binary_array* sub-function.
3. Central point $P(x_0, y_0)$ of C_{nh} is calculated using *detect_central_point* sub-function.
4. Central points $P_n(x, y)$ of other objects present on contour C_{mean} are calculated, where n denotes number of non-connected objects.
5. Algorithm selects two points $P_{RV}(x, y)$ and $P_{LV}(x, y)$ from $P_n(x, y)$ one being to the left and one being to the right of $P(x_0, y_0)$ respectively. Points $P_{RV}(x, y)$ and $P_{LV}(x, y)$ have to satisfy a minimization condition, meaning that their distances r_1 and r_2 to the central point, and angles θ_1 and θ_2 should be minimal (see Fig.27).

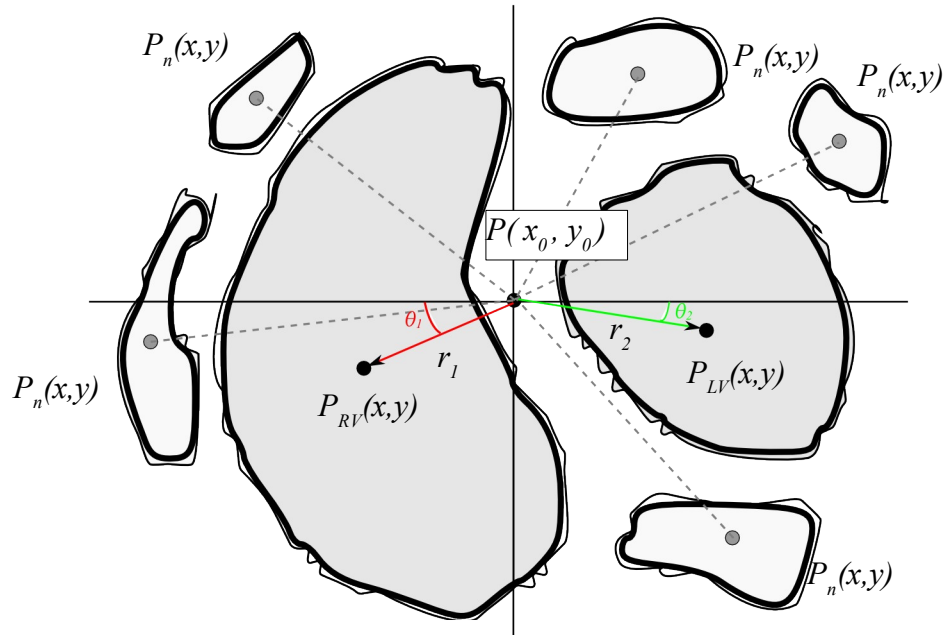


Fig. 27. Detection of right and left ventricle axis points

Using algorithm described above we were able to detect axis points of the ventricles.

Sub-function *dp_array* uses axis points $P_{RV}(x, y)$ and $P_{LV}(x, y)$ to sample contour C equally by θ_s angles with respect to the axis point. We chose sampling angle to be $\theta_s = 0\text{deg}, 5\text{deg}..360\text{deg}$. Obtained sample points $P_{sam}(x, y)$ lie on the edge of the contour C . Cartesian coordinates have been

transformed to polar coordinates to simplify the sampling procedure. Sampled contour of the ventricles is shown in (Fig.28).

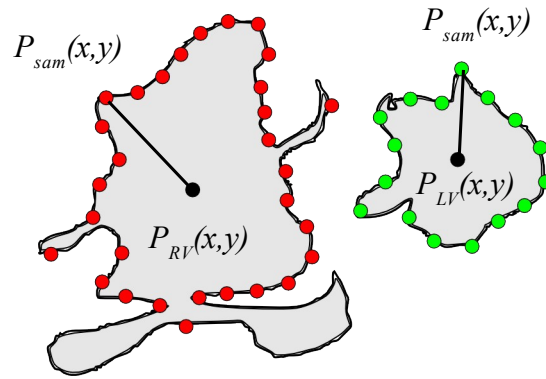


Fig. 28. Contour discretization

Note, that very few sampled points lie in areas with typical artefacts due to contour sparse sampling. Final stage of post-processing would be removal of artefacts from contours C . For that purpose *array_rm_art* sub-function has been implemented. It takes detected contour C which consists of $C_{ventricle} + C_{artifact}$, multitude of sampled points $P_{sam}(x_n, y_n)$, axis points $P_{RV}(x, y)$ and $P_{LV}(x, y)$ as its input values. Output values of the sub-function are left C_{LV} and right C_{RV} ventricle contours. Brief description of the algorithm is following (see Fig.29 left):

1. A loop is initialized for scanning sampled points $P_{sam}(x, y)$ from 1st to nth. Every two points $P_m(x, y)$ and $P_{m-1}(x, y)$ $m \in [2; n]$ are used to plot a straight line r_{max} through them.
2. A sector D_{sector} is formed using r_{max} and $2\theta_{sector}$ as an angle. In our work $r_{max} = 25 \text{ pixels}$ and $2\theta_{sector} = 50 \text{ deg}$ has been chosen.
3. If sampled point $P_{det}(x, y) \in D_{sector}$ then points $P_m(x, y)$ and $P_{det}(x, y)$ will be used as start and end points for an arc $P_m P_{det}$. The arc $P_m P_{det}$ is formed using $P_{RV}(x, y)$ or $P_{LV}(x, y)$ as central point, and distances r_m and r_{det} to points $P_m(x, y)$ and $P_{det}(x, y)$ respectively.
4. Contour C pixel values are set to 0 along the $P_m P_{det}$ arc.
5. New contour $C_{ventricle}$ is obtained as a result of current procedure (Fig.29right).

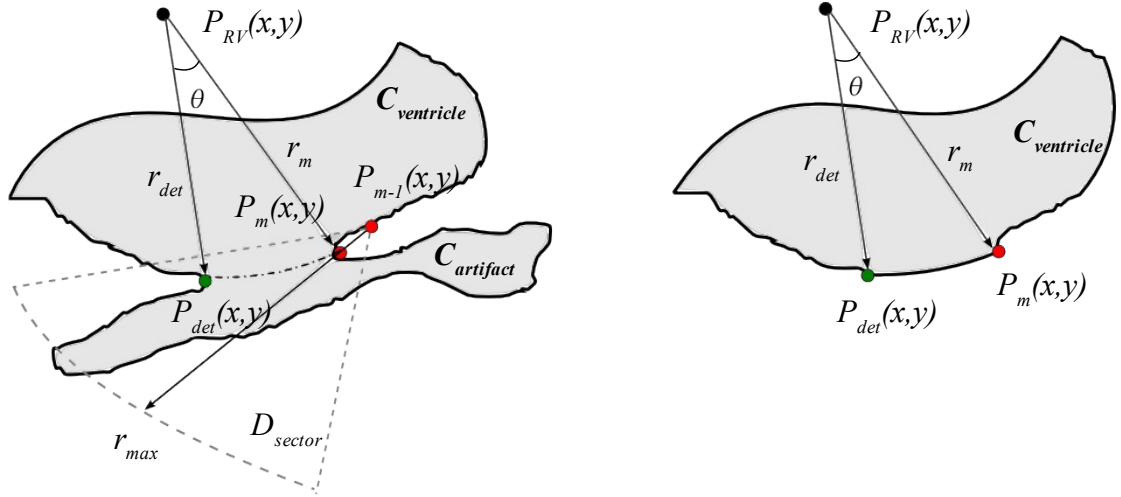


Fig. 29. Cleaning artefacts (left) and new contour (right)

Proposed algorithm allows us to clean contours C of every frame on each slice and obtain ventricle contours C_{LV} and C_{RV} separately from each other. It is possible to restore 3D image of the heart from left C_{LV} and right ventricle C_{RV} contours. It has been done only for demonstration purposes (Appendix 9.1, *r3d.m*) and (Appendix 9.3, Fig.54).

The last step of image processing would be obtaining ventricular volume-time curves from C_{LV} and C_{RV} . Area of contours C_{LV} and C_{RV} for each slice s has been calculated as quantity of bright pixels c_{LV} and c_{RV} inside the

contour times area of the pixel A_{pix} in $\frac{mm^2}{pixels}$:

$$A_{sLV} = A_{pix} c_{LV} , \quad A_{sRV} = A_{pix} c_{RV} \quad (32)$$

Ventricle volumes were obtained as summation of appropriate cylinder volumes by adding up areas of all slices and multiplying them by slice thickness d :

$$V_{LV} = \sum_{s=1}^S A_{sLV} d , \quad V_{RV} = \sum_{s=1}^S A_{sRV} d \quad (33)$$

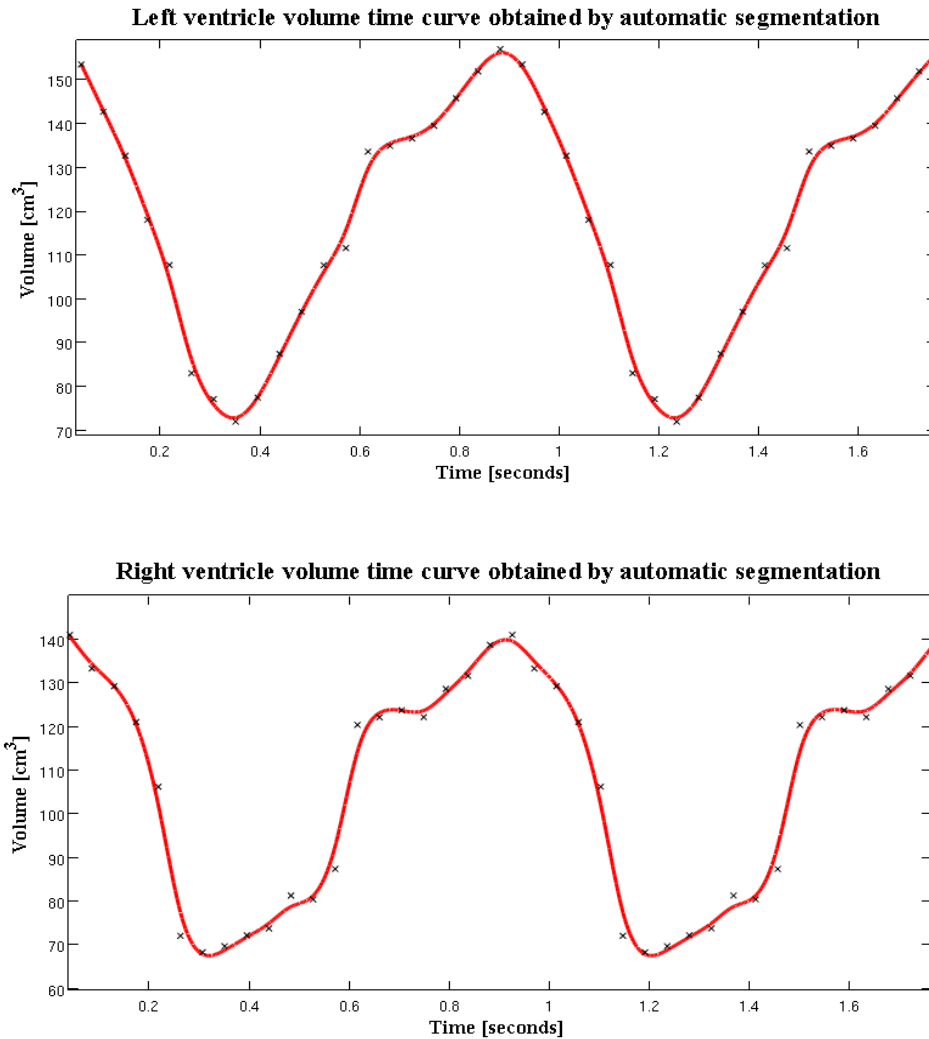


Fig. 30. Left (top) and right (bottom) ventricle volume-time curves obtained by automatic segmentation and smoothed by splines

Curves have been smoothed by cubic spline during the plotting (Fig.30). It has been realized in (Appendix 9.1 *volumefun.m*) programmatically.

3.5 Manual segmentation of MRI images

Images obtained from the cardiac MRI study have been manually segmented also. But firstly images had to be converted from 12 bit DICOM format to standard 8 bit image format. A program *batch8bitconv.m* (Appendix 9.1) has been written to accomplish this. Once images have been converted it was possible to use standard raster image editor to outline a contours around images. This is relatively easy operation for human eye to accomplish since it is able to detect proper edges almost without errors, but since this process includes human factor this makes entire process highly subjective. After segmentation has been completed it was necessary to input segmented images back to MATLAB for further processing with the help of

png_slices_read.m (Appendix 9.1) function. Appropriate slice area and ventricular volume have been calculated using equations (32-33), where C_{LV} and C_{RV} corresponding to manually segmented contours now. Ventricular volume- curves obtained (see Fig.31) were interpolated by cubic splines. Manually and automatically obtained curves are very similar in every respect.

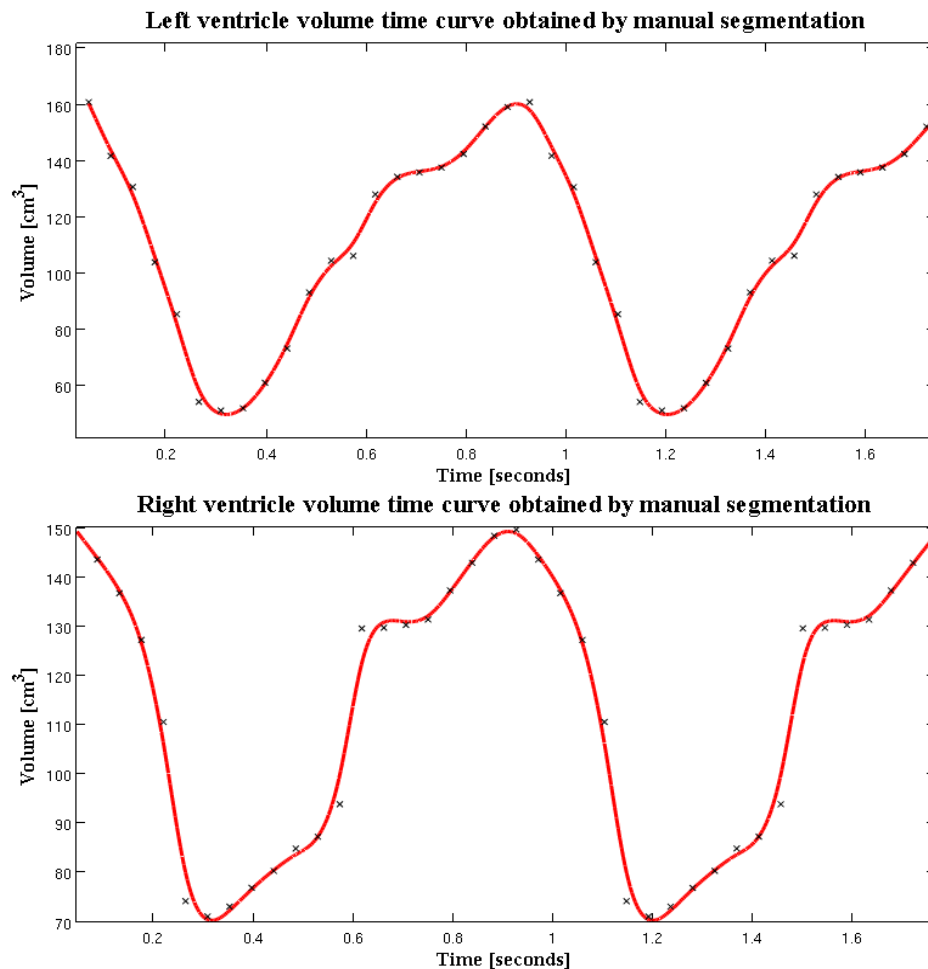


Fig. 31. Left (top) and right ventricle (bottom) volume-time curves obtained by manual segmentation and smoothed by splines

3.6 Foucault cardiogram processing

Recorded raw FouCG signal has a great deal of additive noises at various frequencies and a breathing component. All these noises have been removed using appropriate digital filter combinations (Eqs. 11-14). Following processing flow has been applied to FouCG signal:

1. Read raw ASCII data file and obtain ECG and FouCG data from it.

2. Apply three-point median filter to ECG and FouCG signal to remove impulse noise.
3. Apply Fast Fourier Transform to FouCG signal
4. Apply digital filter $H(\omega)$ to the spectrum part of FouCG. Digital filter has the following construction $|H(\omega)|=0$ if $|\omega|<\omega_c, |\omega|>25$ Hz, 1 otherwise , $\omega_c=0.80$ Hz for the current measurement.
5. Restore signal from its spectrum by applying inverse Fast Fourier Transform.

After filtering and cleaning (used program written in [10]) the FouCG, the signal has presumably only cardiac-originated component left. Ensemble averaged waveform of the FouCG (Fig.32) has been calculated using FCA_II algorithm.

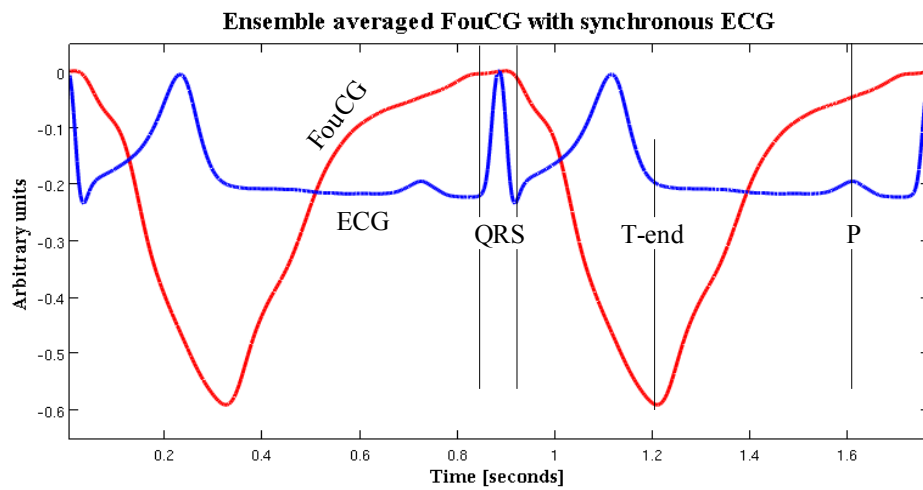


Fig. 32. Ensemble averaged waveform of FouCG with synchronous ECG.

4 DISCUSSION AND RESULT ANALYSIS

4.1 Manual versus active contour segmentation of MRI images

Similarity index for quantitative curve comparison was calculated for various pairs of the signals. Let us compare MRI volume-time curves obtained by automatic segmentation with MRI volume-time curves obtained by manual segmentation (Fig.33). Curves consist of 20 quantization steps. In order to minimize the similarity index calculation error we used cubic-spline interpolation in order to increase the sample rate to 125.

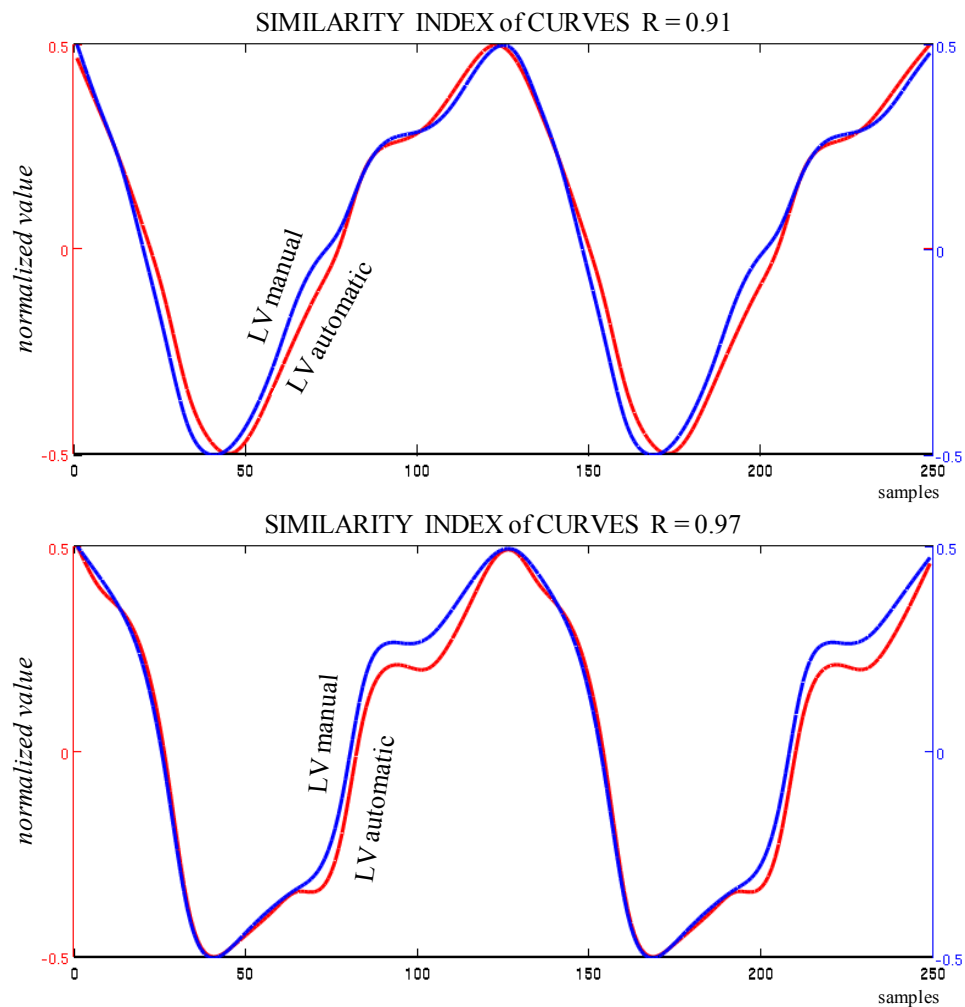


Fig. 33. Similarity index of automatic segmentation method vs manual segmentation method for the MRI LV curve (upper) and the MRI RV curve (bottom).

The partial indexes R_1 and R_2 for the 1st and 2nd order derivatives of the signal can be seen in (Appendix 9.3, Figs. 48-51). It is clearly noticeable that curves obtained by different methods are qualitatively the same. We have obtained similarity indices of 0.91 and 0.97 for LV and RV comparison respectively. It can be noted, that

similarity index for LV is a bit lower because of the systolic minimum shift. The shift described could appear due to subjective error made by human operator while segmenting the heart in the end of systole.

There is a difference in stroke volumes between left and right ventricles in 13cm^3 , obtained during automatic segmentation, and 28cm^3 , obtained during manual segmentation respectively (Fig.34). We assume, that this deviation occurred because of imaging planes tilt in the horizontal long axis image (Fig.14 right), which resulted in cardiac valve plane proper identification error. Secondly, we have not taken into account the cardiac plane valve shift during heart contraction. The boundary imaging plane locations during systole and diastole were the same. Stroke volume obtained from manually segmented images resulted to be greater, because we have included papillary muscles to the volume calculations. Shape of the LV curve obtained is very similar to Z. Zeidan et al. research paper [16], which allows us to conclude that derived waveform is correct.

	Automatic segmentation		Manual segmentation	
Ventricle	Left	Right	Left	Right
Stroke volume	83cm^3	70cm^3	108cm^3	80cm^3

Fig. 34. Stroke volumes

Based on the current results it can be concluded that algorithm programmed in MATLAB environment is highly robust and efficient. As it turned out, the drawback of the current algorithm is in inability to determine the cardiac valve plane properly, resulting in difference of stroke volumes of the ventricles. Despite this, we can conclude that the active contour method proposed is highly suitable for cardiac MRI images segmentation with 94% confidence.

4.2 Comparison of ejection fractions obtained from MRI and Ultrasound

Let us compute ejection fractions obtained from MRI and Ultrasound and present results as a table (Fig.35). Ejection fractions obtained does not differ much from each other, thus allowing us to speak about certain similarities in results produced by different methods. LV and RV ejection fractions obtained from MRI scanning are within 5% difference compared to ultrasound measurement. In its turn whole heart ejection fraction obtained from MRI is within 3% difference compared to

echo. Right ventricle EF, ESV, EDV values are in good correspondence with A. Maceira et al. paper [26].

	MRI		Ultrasound	
Ventricle	Left	Right	Left	Right
Ejection fraction	68.00%	53.00%	67.00%	58.00%
Ventricle	Sum of ventricles		Sum of ventricles	
Ejection fraction	60.00%		62.50%	

Fig. 35. Comparison of MRI ejection fraction with Ultrasound ejection fraction.

Comparison of ejection fractions obtained from different methods allows us to conclude following: MRI measurement protocol has been prepared correctly and provides accurate results; ESV and EDV have been obtained correctly from MRI image processing algorithm.

4.3 Volume-time curve from segmented MRI images versus FouCG averaged waveform

Let us compare FouCG with MRI LV, RV and LV+RV volume-time curves on the assumption that the MRI is a precise method and can be considered as the standard. FouCG is believed to be less trustworthy method, because of lack of calibration against volume units and arbitrary bias of the signal against Y-axis. The positive moment of FouCG lies in similarity of its waveform to ventricular volume curve from medical books. We want to interpret the FouCG signal as changes in ventricular volume. Comparison of ensemble averaged FouCG waveform with MRI curves helps us to conclude if the FouCG signal allows to track ventricular volume.

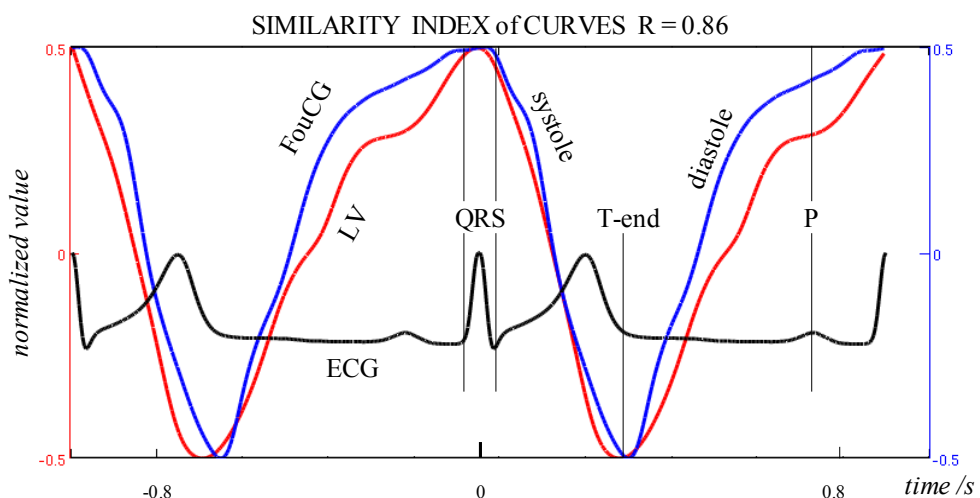


Fig. 36. Comparison of LV MRI volume-time curve with FouCG

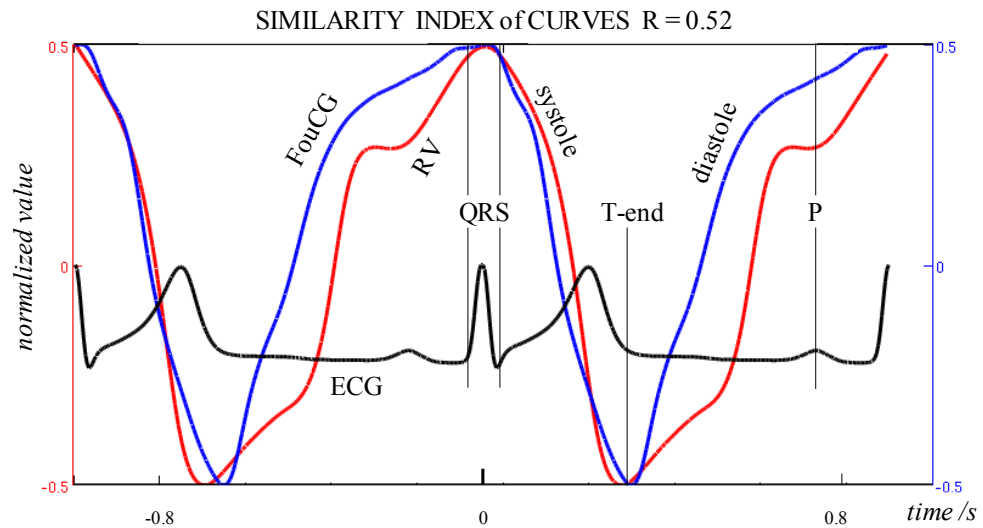


Fig. 37. Comparison of RV MRI volume-time curve with FouCG

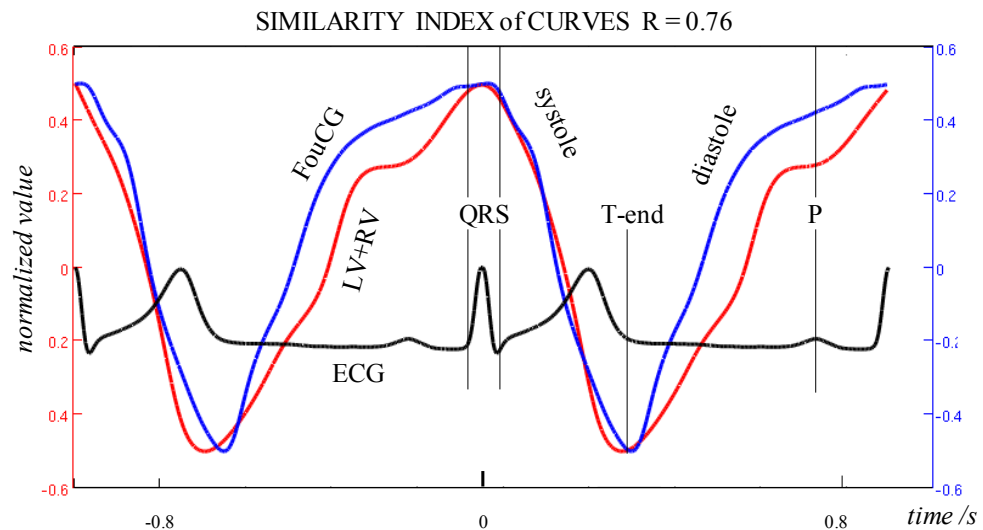


Fig. 38. Comparison of the sum of both ventricle volume-time curves with FouCG

In the process of comparison, the extents of the curves were normalized to 1 and couples of the FouCG and MRI signal cycles were matched at the centre of the ECG R-wave. Due to a small difference of the heart periods, MRI and FouCG curves showing slight desynchronization with the increase in time distance from the matching point. FouCG versus MRI LV, RV and LV+RV volume curve partial indices R_1 and R_2 are plotted in (Appendix 9.3 Figs. 52-57) respectively.

Quantitatively the highest similarity index of 0.86 (Fig.36) between the FouCG and MRI volume-time curve was obtained for the LV. At the early systole stage the curves show almost similar behaviour. A small difference can be seen at the end of the QRS complex: the FouCG exhibits decrease of incline, while the MRI curve declines a bit faster. Inclines of the both curves exhibit similar behaviour by the

end of ST interval (end-systole). During the early diastole, blood starts to enter ventricle and its volume extends. Again FouCG shows more rapid increase than the MRI LV. By the end of TP segment (end-diastole) there is a noticeable difference between the FouCG and MRI LV curve. The FouCG signal amplitude is greater than of the LV curve. This behaviour should be considered as incorrect, since rapid ventricular volume increase should take during the PR segment only. MRI reflects the ventricular behaviour during PR segment more accurately. One of the reasons can be in suffering of FouCG signal from the cardiopulmonary interference, which appears as displacement of the heart during volume changes of lungs. Ensemble averaging of FouCG signal with cardiopulmonary interference could affect the diastolic part of the recorded signal more. MRI is free from cardiopulmonary interferences because we implemented countermeasures like breath-holding technique. In defence of FouCG it can be said that it also shows increase in signal amplitude during PR segment (end-diastole) as the MRI does. FouCG reflects isovolumic contraction (the time interval between the mitral valve closes and aortic valve opens) at R wave more accurately. It can be seen that FouCG does not increase nor decrease considerably during this process. The MRI LV curve simply has not been sampled frequently enough to show that behaviour.

Similarity index between the MRI RV and FouCG is 0.52 (Fig.37). There is relatively low similarity between these two curves according to the index. Both the MRI RV and FouCG curves reflect similar physiological processes described above, having significant deviation in the diastolic process, which only reduces at the beginning of the Q wave. During systolic process both curves are quite similar.

Similarity index between the MRI LV+RV (i.e. at equal contributions by the both) and FouCG is 0.76 (Fig.38). Again the curves are virtually similar during systole stage both in behaviour and magnitude, but increasing difference arises during diastole stage, when FouCG magnitude increases faster. Thus, the contribution of the RV into FouCG should to be less than 50%, because similarity has rather greatly decreased when 50% contribution of RV has been introduced.

It is reasonable to assume, that both ventricular components of LV and RV are present in the FouCG. Still it turned out, that influence of the LV is much greater than of RV. The reason for this feature might be in position of the heart ventricles in thorax and the fact that the eddy currents weaken with the distance from the inductor too much to penetrate deeper inside the body. If we take a closer look at (Fig.17) again,

we will see, that LV occupies greater area on coronal image than RV if patient is lying on the back. It can be said that RV is “under” LV due to heart position in human body. That can be one of the reasons why the Foucault cardiograph inductor placed on the patient's chest will measure LV activity more than RV activity. RV being distanced greatly from inductor will influence the measured signal less.

Since blood is ejected from the heart during systole, its ventricular volume decreases during that phase. The FouCG signal shows decrease of amplitude during systole very accurately. Drawback of FouCG here is in its inability to reflect the diastolic process accurately. We can suggest a hypothesis, that diastolic FouCG signal gets distorted because Foucault cardiograph senses not only blood outflow or inflow inside the heart, but also its displacement during the cardiac cycle. The MRI curves do not suffer from this displacement since it was eliminated at the image segmentation stage and the technique of measurement. Still, FouCG signal does depict diastolic phase by additional increase in its value, allowing us to conclude that the signal reacts to the blood inflow together with possible displacement of the heart.

Unfortunately we were unable to assess cardiac displacement in the MRI images we had already. This requirement has not been simply foreseen at the beginning and lies outside of the problem scope. We can suggest studying this problem further if not with MRI (due to its operational cost and overall complexity), then with 3D ultrasound techniques currently widely available.

Another problem discovered during our study is that the Foucault cardiograph records a great deal of radio frequency noises, when used at the hospital. This leads us to believe, that its construction is not shielded properly enough. Secondly, if Foucault device is going to be used at the hospital for radiological measurements it has to comply with electrical safety standards, proper certification might be required. Thirdly, the overall weight of apparatus should be greatly reduced to increase its usability. But these are the topics for future efforts.

To support our theory, we recorded additional raw FouCG from the same volunteer. Compared to the previous recording we have placed the device inductor so that both ventricles influenced the signal in the similar manner (see Fig.39).

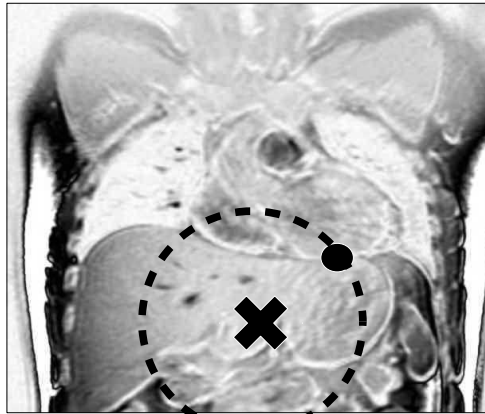


Fig. 39. Position of the Foucault inductor during 2nd recording.

Let us present comparison of processed 2nd and ensemble-averaged FouCG waveform with ventricular volume-time curves we already have. LV similarity index (Fig.40) is still very high, being 0.75 in value. However, as it could be predicted RV similarity (Fig.41) increased compared with previous FouCG. Distinctive feature of RV behaviour could be seen in FouCG also (shown by dashed circle). The most important result of second measurement is in highest similarity index obtained for the sum of ventricular curves (see Fig.42), which again confirms presence of LV and RV volumetric components in FouCG. Contribution of RV is higher for the current position of the Foucault inductor compared to the FouCG initial recording. To sum up we can hypothesize that FouCG can be described by the following equation:

$$FouCG = \alpha LV_{vol} + \beta RV_{vol} + \gamma (LV_{disp} + RV_{disp}) ,$$

where α , β , γ - are the weights depending on the Foucault inductor position; *vol* – volumetric component; *disp* – displacement component.

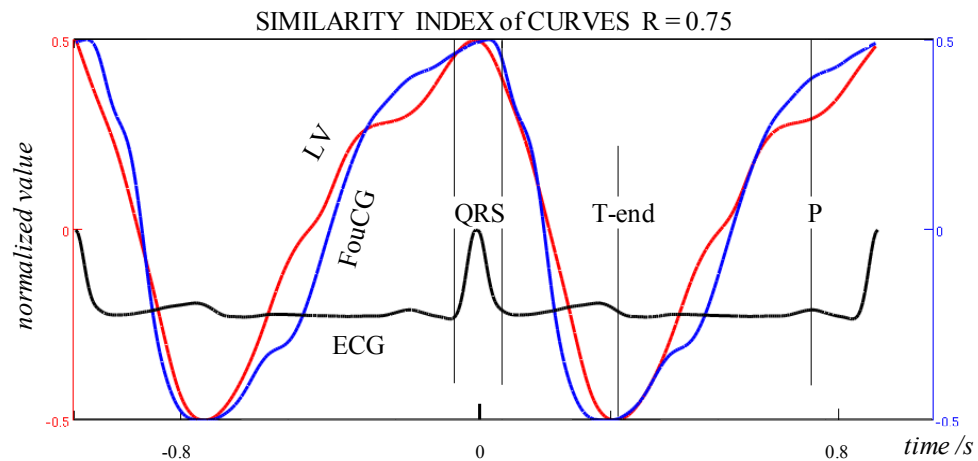


Fig. 40. Comparison of LV MRI volume-time curve with 2nd FouCG

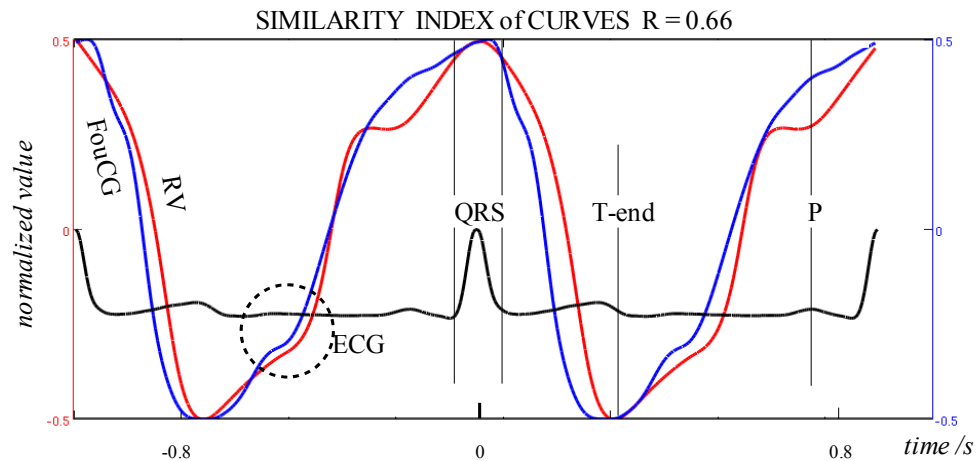


Fig. 41. Comparison of RV MRI volume-time curve with 2nd FouCG

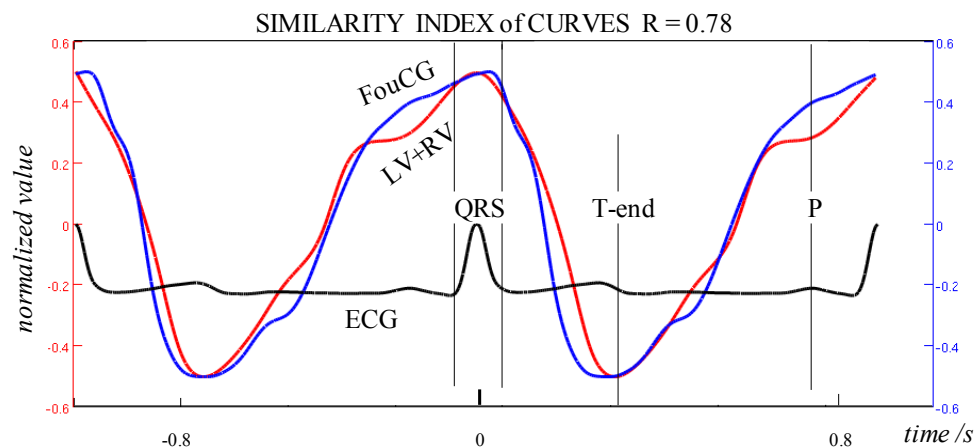


Fig. 42. Comparison of the sum of both ventricle volume-time curves with 2nd FouCG

4.4 Future efforts

For improvement and studies continuation on the topic we propose following:

- Develop better and more reliable FouCG equipment in order to allow conduction of clinical studies
- Optimize cardiac MRI study procedure in order to allow acquisition of required images in least possible research time.
- Improve MRI images segmentation algorithm to increase its robustness, speed and ability to work with various data.
- Attempt to calibrate FouCG signal according to MRI.
- Attempt to study contraction-associated cardiac displacement using MRI or 3D ultrasound techniques.

5 CONCLUSIONS

Our study showed that FouCG waveform resembles similarity with ventricular blood content in ejection and filling process. We have observed deviation of FouCG from the corresponding MRI curves during diastole and attempted to explain it. Still it is likely that FouCG enables monitoring of systolic ventricular hemodynamics. Diastolic ventricular hemodynamics is not being represented accurately enough by FouCG especially at ECG's P-wave due to possible a possible displacement of the heart towards the transducer. Therefore, tracking relative variation of stroke volume and associated quantities should be possible in clinical applications. The successfully achieved goals of this thesis are listed below:

1. Cardiac MRI study has been planned and conducted thoroughly with support of West Tallinn Central Hospital.
2. Foucault cardiographic measurements have been conducted with the same patient, trying to repeat his physical conditions.
3. Digital image processing algorithm, suitable for automatic processing and segmentation of MRI images has been developed.
4. Algorithm implementation has been written as MATLAB 2010 application. Volume-time curves for the left and right ventricles have been separately obtained from digital images.
5. FouCG signal has been processed and cleaned from unwanted noises and components. Ensemble averaged FouCG waveform has been calculated.
6. Ensemble averaged FouCG waveform has been compared with left ventricle, right ventricle and both ventricles volume-time curves obtained from MRI study. Similarity indexes based on signal-itself, 1st and 2nd derivative correlation components have been calculated.
7. Results have been analysed and possible explanation in differences between FouCG method and MRI made.

6 SUMMARY

COMPARISON OF FOUCAULT CARDIOGRAM WITH MRI VENTRICULAR VOLUME-TIME CURVE

Grigori Savustjan

The present study has been performed as co-operation of Faculty of Science and Technology of the University of Tartu and West Tallinn Central Hospital. Master's thesis belongs to the field of biomedical engineering, medical physics, image processing and signal processing. Topic considers fundamental problem of Foucault cardiography and its aim is to clarify the ability of the method to represent physiological processes of ventricular mechanical activity.

Comparison referred in the title was undertaken in order to clarify the ability of the FouCG method to represent physiological processes of ventricular mechanical activity. We have conducted cardiac MRI study and calculated ventricular volume-time curves from digital images. To achieve the objectives appropriate software has been developed in MATLAB numerical computing environment. Firstly an algorithm capable of automatic detection of the heart in MRI images has been implemented. At the second stage algorithm utilizes found location of the heart and segments images using Chan-Vese active contour implementation. Contours are then cleaned with special algorithms and the ventricular volume-time curves are calculated. Foucault cardiogram has been cleaned of any non-cardiac originated components using digital filters and ensemble averaged waveform obtained.

It was shown that automatic segmentation algorithm of cardiac MRI images provides as good results as manual segmentation by skilled operator.

To compare volume-time curve obtained from MRI study with the ensemble averaged Foucault cardiogram a similarity index was utilized. According to calculated values of the similarity indices it turned out, that FouCG resembles mechanical activity of the left ventricle with considerably higher confidence. Right ventricle contribution to the FouCG is lower, but still present. We assumed, that FouCG could be used to monitor at least the systolic mechanical activity of the left ventricle in clinical applications. In our opinion, it is necessary to develop better and more reliable FouCG equipment and to continue with studies of patients in parallel with cardiac MRI studies at the hospital to assess every shortcomings of the method.

7 KOKKUVÕTE

FOUCAULT' KARDIOGRAMI JA MRT-GA SAADUD VATSAKESTE RUUMALA KÕVERA VÕRDLEMINE

Grigori Savustjan

Käesolev magistritöö teostati koostööna Tartu Ülikooli Loodus- ja Tehnoloogiateaduskonna ning Lääne-Tallinna Keskhaigla vahel. Väitekiri kuulub biomeditsiinitehnika, meditsiinifüüsika, pilditöötuse ja signaalitöötuse valdkonda. Teema käsitleb fundamentaalset probleemi Foucault kardiograafias, milleks on teha selgeks meetodi võimalust jälgida füsioloogilisi protsesse mis toimuvad südame vatsakeste mehhaanilist tegevuse tõttu.

Pealkirjas viidatud võrdlus viidi läbi, et välja selgitada FouKG meetodi võimalusi vatsakeste mehaanilise tegevuse edasiandmiseks. Südame MRT uuring viidi läbi, et selles registreeritud pildiseeriade põhjal välja arvutada vatsakeste ruumala muutmise tsükli kõver. Eesmärgi saavutamiseks töötati spetsiaalne MATLABi tarkvara. Arvutuse esimesel etapil leitakse registreeritud MRT andmete põhjal, mida tõlgendatakse 4D-massiivina, südame asukoht. Algoritmi järgmine osa kasutab leitud asukohta lähtena ja segmenteerib 2D MRT-kujutised Chan-Vese aktiivsete kontuuride meetodil. Seejärel korrastatakse leitud südame lõigete kontuurid spetsiaalselt selleks väljatöötatud algoritmiga ning nende põhjal arvutatakse välja vastavad parema ja vasaku vatsakese ruumala kõverad. Töös on näidatud, et MRT kujutiste automaatse segmenteerimise algoritm annab peaaegu samad tulemused nagu kujutiste segmenteerimine inimoperaatori poolt.

Foucault kardiogrammist (FouKG) eemaldati kõik südametegevusega mitte seotud komponendid ja leiti ansamblikeskmise lainekuju. FouKG ja MRT kõverate sarnasuse hindamiseks kasutati sarnasuse näitajat. Sarnasuse indeksi leitud väärtuste põhjal on tehtud järeldus, et FouKG esitab tugevamini vasaku vatsakese mehhaanilist tegevust. Parema vatsakese panus FouKG signaali on olemas, kuid on väiksem. Võib järelda, et FouKG meetodit võiks kasutada vähemalt vasaku vatsakese süstoolse mehhaanilise tegevuse jälgimiseks kliinilistes uuringutes.

Töös esitatakse soovitus täiustada FouKG aparatuuri, et jätkata meetodi edasisi uuringuid haigete uurimisega, paralleelselt uuringutega patsientidel, kes läbivad südame MRT-uuringuid.

8 BIBLIOGRAPHY

- [1] L-H. Humal, J. Vedru, "Physiological Measurement Based on Foucault Principle: Setup of the Problem," *Medical & Biological Engineering & Computing*, 1996; 34, 1, 2, pp. 183-184.
- [2] P.P. Tarjan, R. McFee, "Electrodeless Measurement of the Effective Resistivity of the Human Torso and Head by Magnetic Inductions," in *IEEE Trans. on Bio-Medical Eng.* 1968; Vol. BME-15, No.4, pp. 266-278.
- [3] C.J. Wiggers, L. N. Katz, "The contour of the ventricular volume curves under different conditions", *Am. J. Physiol.* 58, 1922; pp. 439-475.
- [4] J. Vedru, "Electrical impedance methods for the measurement of stroke volume in man: state of art," *Acta et Comm. Univ. Tartuensis*, 1994; No 974, pp. 110-129.
- [5] J. Malmivuo, R. Plonsey, "Bioelectromagnetism - Principles and Applications of Bioelectric and Biomagnetic Fields," *Oxford University Press, New York*, 1995.
- [6] J. Vedru, J. Trolla, P. Loog, J. Talts, "Prospect of Foucault cardiography for the monitoring of cardiac output," *Proc. Int. Conf. Biomedical Engineering*, Kaunas, 22-23 October 1998; pp. 12-15.
- [7] J. Vedru, J. Trolla, L.-H. Humal, V. Lugna and S. Vesselova. "Magnitude Distribution of Foucault Cardiogram on Human Thoracic Surface," *Medical & Biological Engineering & Computing*, 1999; Vol. 37, Suppl.1 pp. 251-252.
- [8] J. Vedru, O. Makarova, V. Tina, "Averaged Waveforms of Electrical Bioimpedance: Construction and Comparison," *Proc. XI Int. Conf. Electrical Bio-impedance*, Oslo, 2001, pp. 631-635.
- [9] N. Tchironova, "Comparison of possibilities of tracking the heart volume using MRI and Foucault cardiography," *Bachelor's thesis*, Univ. of Tartu, 2005.
- [10] G. Savustjan, "Separation of ventricular rate from the heart rate in Foucault cardiogram," *Bachelor's thesis*, Univ. of Tartu, 2005.
- [11] V. Zadin, K. Skaburskas, J. Vedru, "Influence of Breathing on Foucault Cardiogram Origination," *13th Int. Conf. on Electrical Bioimpedance and*

- 8th Conf. on Electrical Impedance Tomography*, Graz, Austria, Aug. 29 - Sept. 2, 2007; Vol. 17. pp. 62 – 65.
- [12] O. Tarassova, J. Vedru, “Possibilities of Foucault Cardiography-Based Estimation of Heart Pumping Performance,” *13th Int. Conf. on Electrical Bioimpedance and 8th Conf. on Electrical Impedance Tomography*, Graz, Austria, Aug. 29 - Sept. 2, 2007; Vol. 17. pp. 586 – 589.
- [13] J. Vedru J, O. Solntseva, “Variation of Magnetic Induction Plethysmogram on Human Thoracic Surface,” *13th Int. Conf. on Electrical Bioimpedance and 8th Conf. on Electrical Impedance Tomography*, Graz, Austria, Aug. 29 - Sept. 2, 2007; Vol. 17. – Pp. 743 - 746.
- [14] J. Trolla, J. Vedru, “On the Safety of Foucault Cardiography,” *Proc. XI Int. Conf. Electrical Bio-impedance*, Oslo, 2001; pp. 649-652.
- [15] N. Ovetchko, N. Tchironova, R. Ollik, R. Kivimäe, J. Vedru, “Ascertaining the link between the heart motion and Foucault cardiogram,” *Proc. Int. Conf. Biomedical Engineering, Kaunas, Oct. 2005*, Kaunas, 2005; pp. 115-118.
- [16] Z. Zeidan, R. Erbel, J. Barkhausen, P. Hunold, T. Bartel, T. Buck, “Analysis of Global Systolic and Diastolic Left Ventricular Performance Using Volume–time Curves by Real-time Three-dimensional Echocardiography,” *Journal of the American Society of Echocardiography*, 2003; Vol 16, No.1
- [17] M. García de Pablo, N. Malpica, M-J Ledesma-Carbayo, L-J Jiménez-Borreguero, A. Santos, “Semi Automatic Estimation and Visualization of Left Ventricle Volumes in Cardiac MRI,” *Computers in Cardiology* 2005; 32 pp. 399–402.
- [18] W. Soergel, V. Vaerman, “Automatic heart localization from a 4D MRI dataset,” *Medical imaging 1997. Conference*, 1997; vol. 3034 (2), pp. 333-344.
- [19] Y. Wu, “Chan-Vese Active Contours without edges,” <http://www.mathworks.com/matlabcentral/fileexchange/23445-chan-vese-active-contours-without-edges>
- [20] Hsun-Hsien Chang, Jose M. F. Moura, Yijen L. Wu, and Chien Ho, “A mutual information approach to automatic detection of heart rejection in MRI,” *Proc. 14th Annual Meeting of International Society of Magnetic*

- Resonance in Medicine (ISMRM '06), Seattle, WA, May 6-12, 2006, p. 1199
- [21] M. Mustra, M. Grgic, K. Delac, "Efficient Presentation of DICOM Mammography Images using Matlab," *15th International Conference on Systems, Signals and Image Processing*, 2008; pp. 13 – 16.
- [22] F. Jamali Dinan, P. Mosayebi, H. Abrishami Moghaddam, M. Giti, "A dynamic surface model for segmentation of cardiac MRI images and its usage in cardiac wall motion tracking," *Measurement science review*, 2007; Vol. 7, Sec. 2, No. 1.
- [23] J-L. Wang, W-Y. Isaac Tseng, T-Y. Liao, "A robust edge detection algorithm for volumetric analysis of left ventricle in cine MRI," *Biomed. Eng. Appl. Basis. Comm.*, 2000; 12; pp. 75-80.
- [24] J. P. Earls, V. B. Ho, T. K. Foo, "Cardiac MRI: Recent progress and continued challenges," *J. Magn. Reson. Imaging* 2002;16, pp. 111–127
- [25] N. G. Bellenger, M. I. Burgess, S. G. Ray, A. Lahiri, A. J. S. Coats, J. G. F. Cleland and D. J. Pennell, "Comparison of left ventricular ejection fraction and volumes in heart failure by echocardiography, radionuclide ventriculography and cardiovascular magnetic resonance," *European Heart Journal*, 2000; 21, pp. 1387–1396.
- [26] A. M. Maceira, S. K. Prasad, M. Khan, D. J. Pennell, "Reference right ventricular systolic and diastolic function normalized to age, gender and body surface area from steady-state free precession cardiovascular magnetic resonance," *European Heart Journal* 2006; vol. 27, pp. 2879–2888.
- [27] N. Otsu, "A Threshold Selection Method from Gray-Level Histograms," *IEEE Transactions on Systems, Man, and Cybernetics*, Vol. 9, No. 1, 1979, pp. 62-66.
- [28] S. Zambal, A. Schoellhuber, K. Buehler, J. Hladuvka, "Fast and robust localization of the heart in cardiac MRI series," *Proc. Int. Conf. on Computer Vision Theory and Applications*, 2008; pp. 314-316.
- [29] T. Chan, L. Vese, "Active contours without edges," *IEEE Transactions on image processing*, 2001; Vol. 10, No. 2, pp. 266-277.
- [30] M. Kass, A. Witkin, D. Terzopoulos, "Snakes: Active contour models," *International Journal of Computer Vision*, 1987; pp. 321-331.

- [31] L. D. Cohen, "On active contour models," *Robotics, image and vision*; 1989, Vol. 6, No. 1075.
- [32] T. McInerney, D. Terzopoulos, "Deformable models in medical image analysis: A survey," *Medical Image Analysis*, 1996; 1(2): pp. 91–108.
- [33] R.C. Gonzalez, R.E. Woods and S.L. Eddins, "Digital Image Processing Using Matlab," *Pearson Prentice Hall, New Jersey*, 2004
- [34] J. L. Semmlow, "Biosignal and biomedical image processing: Matlab based applications," *Signal processing and communication series*, 2004.
- [35] "DICOM: Information Object Definitions," *National Electrical Manufacturers Association* 1300 N. 17th Street Rosslyn, Virginia 22209 USA

9 APPENDICES

9.1 MATLAB program code (on a compact disc)

9.2 Processed images

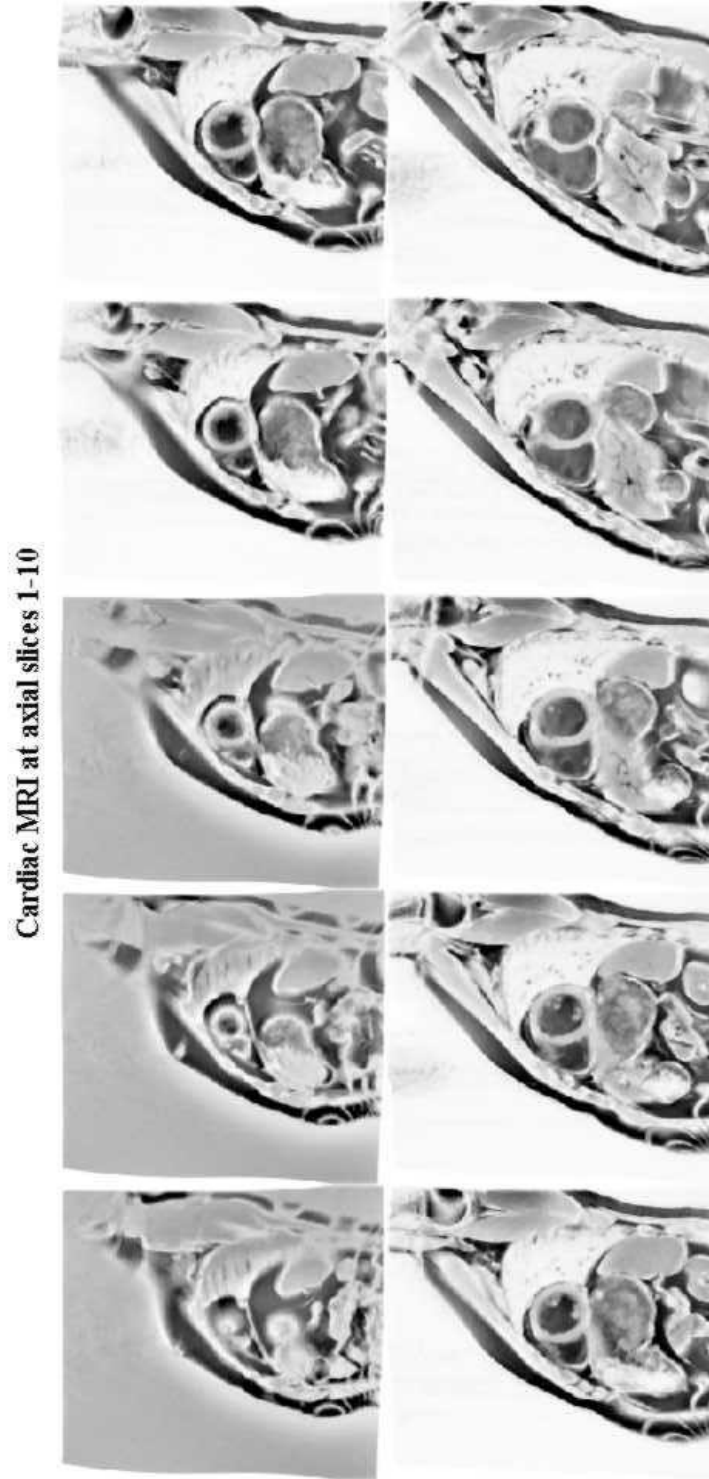


Fig. 43. Original cardiac MRI images at axial slices 1-10

Temporal mean images at slices 1-10

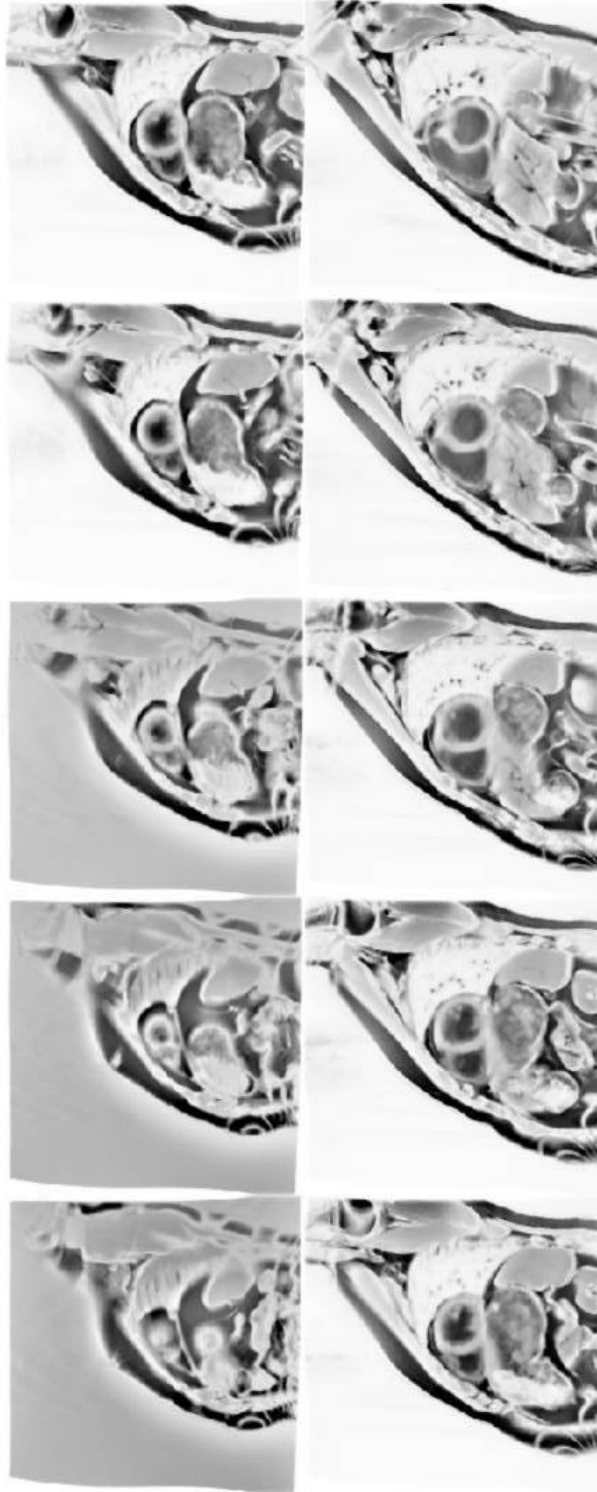


Fig. 44. Temporal mean images for each axial slice 1-10

Variance images at axial slices 1-10

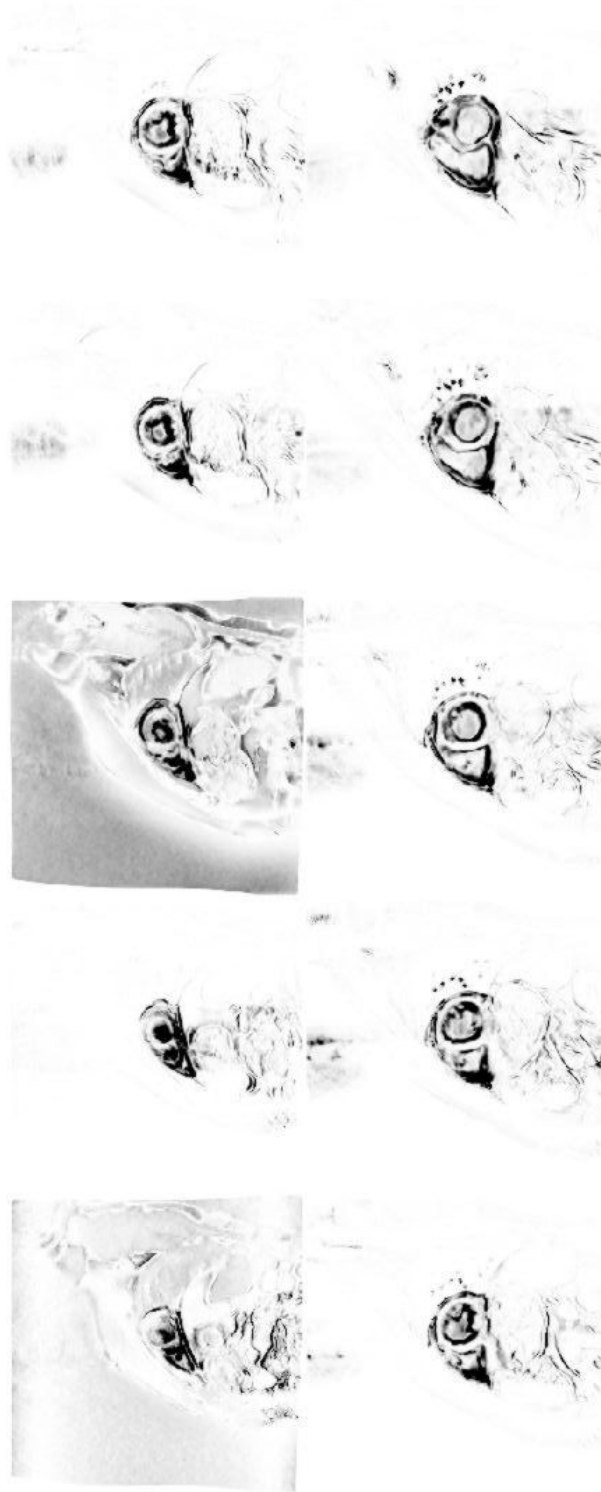


Fig. 45. Variance images for each axial slice 1-10

Binarized variance images at axial slices 1-10



Fig. 46. Thresholded variance images for each axial slice 1-10

Cleaned binarized variance images at axial slices 1-10



Fig. 47. Variance images for each axial slice 1-10

9.3 Figures

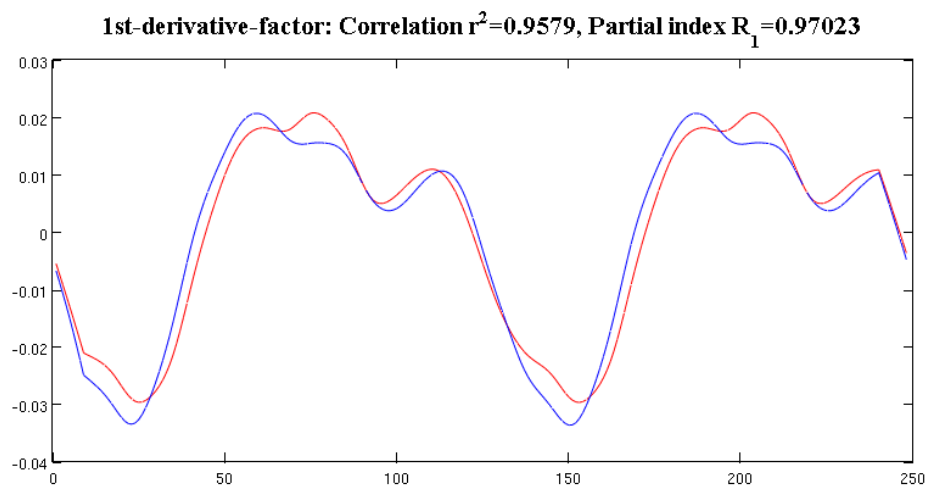


Fig. 48. Correlation of 1st derivative of LV curve obtained by automatic segmentation vs 1st derivative of LV curve obtained by manual segmentation.

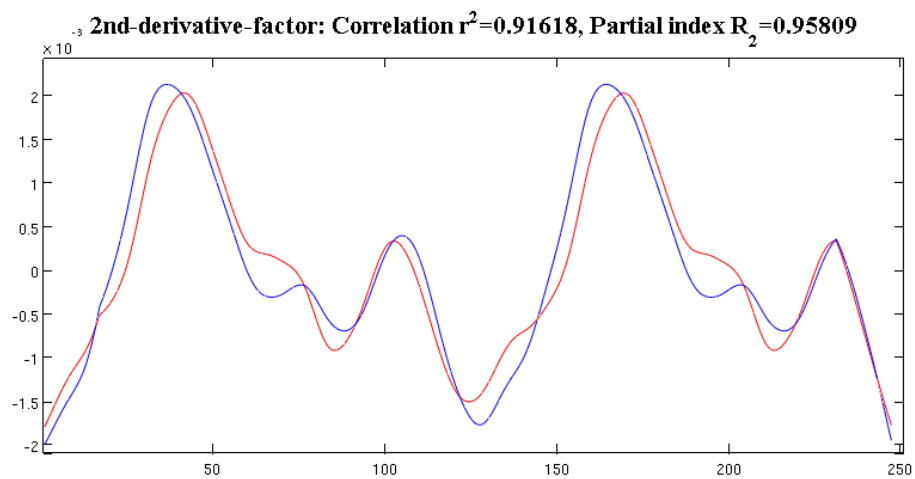


Fig. 49. Correlation of 2nd derivative of LV curve obtained by automatic segmentation vs 2nd derivative of LV curve obtained by manual segmentation.

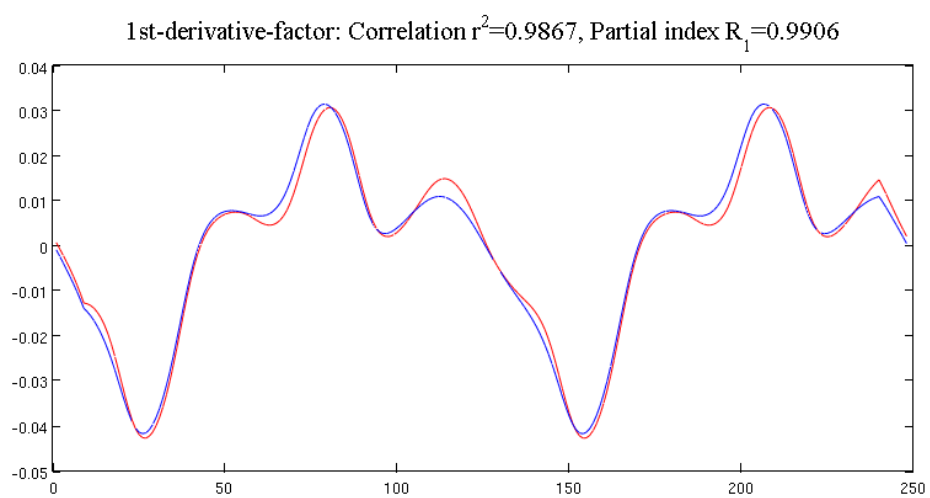


Fig. 50. Correlation of 1st derivative of RV curve obtained by automatic segmentation vs 1st derivative of RV curve obtained by manual segmentation.

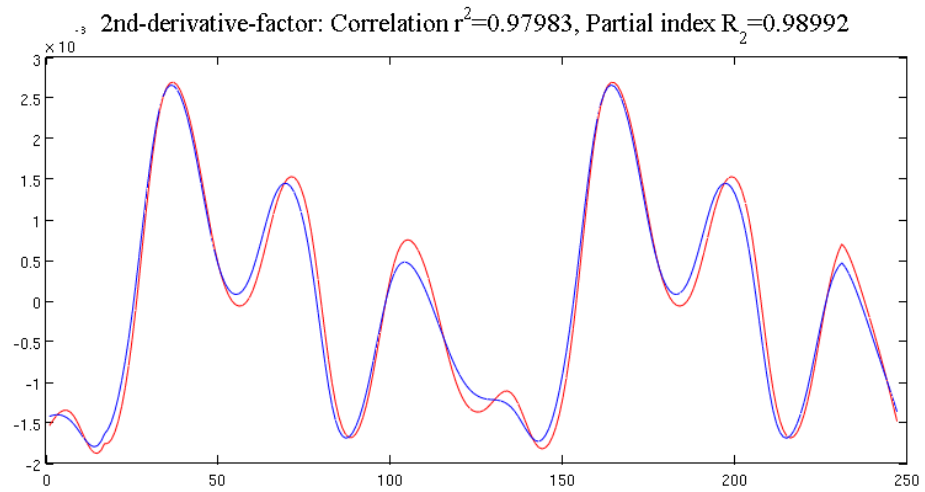


Fig. 51. Correlation of 2nd derivative of RV curve obtained by automatic segmentation vs 2nd derivative of RV curve obtained by manual segmentation.

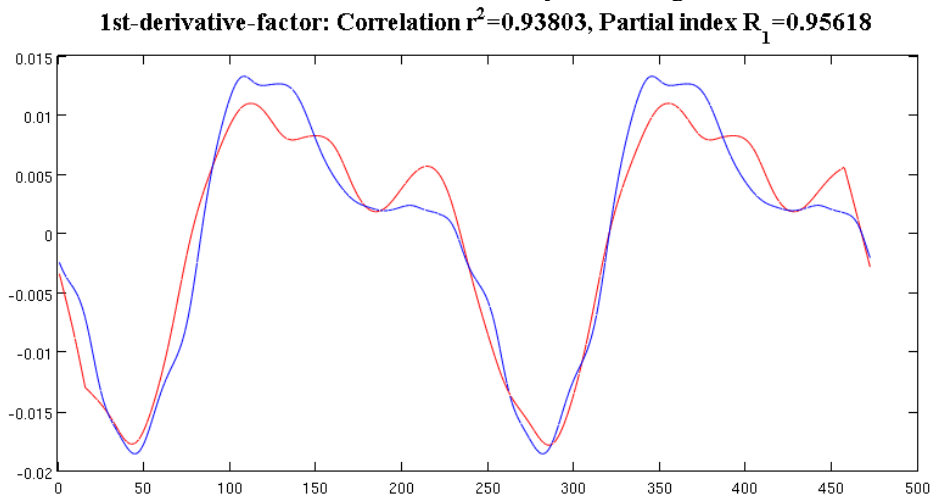


Fig. 52. Correlation of 1st derivative of LV curve obtained by automatic segmentation vs 1st derivative of ensemble averaged FouCG

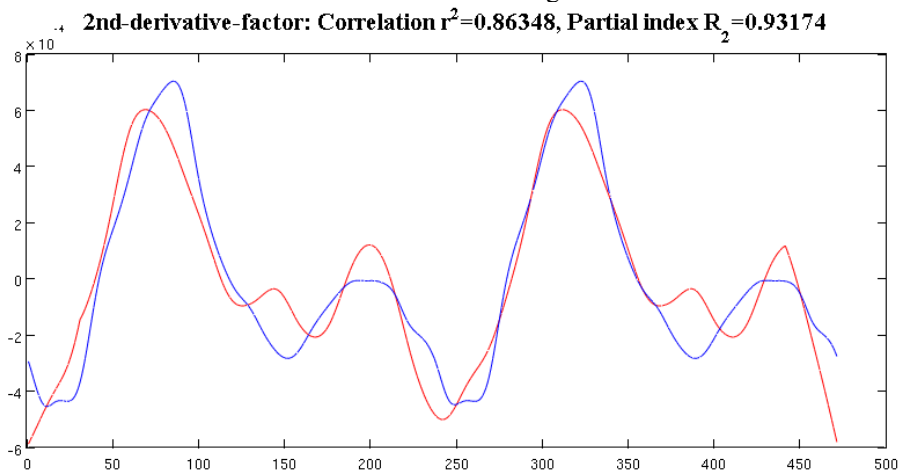


Fig. 53. Correlation of 2nd derivative of LV curve obtained by automatic segmentation vs 2nd derivative of ensemble averaged FouCG

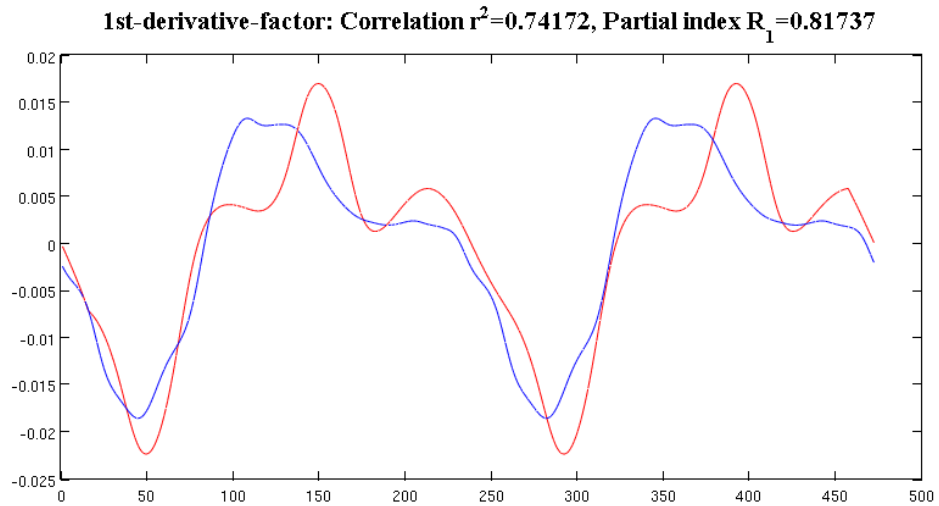


Fig. 54. Correlation of 1st derivative of RV curve obtained by automatic segmentation vs 1st derivative of ensemble averaged FouCG

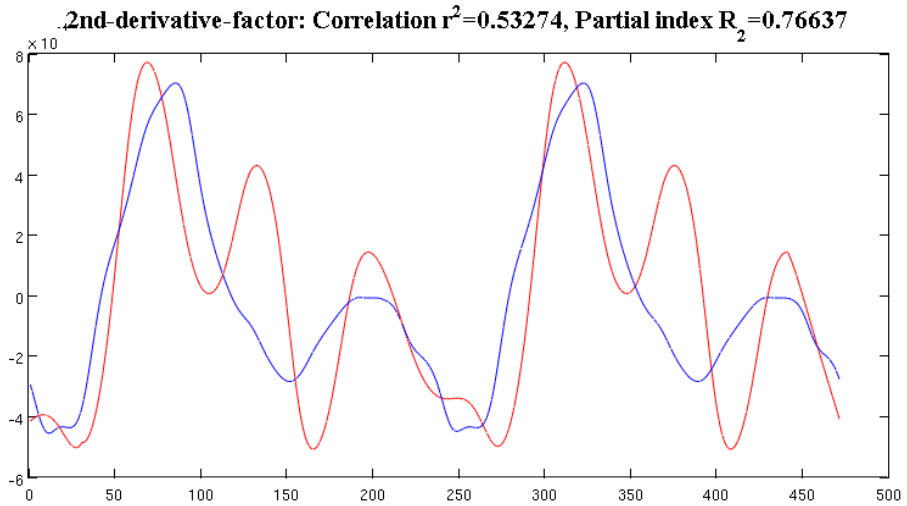


Fig. 55. Correlation of 2nd derivative of RV curve obtained by automatic segmentation vs 2nd derivative of ensemble averaged FouCG

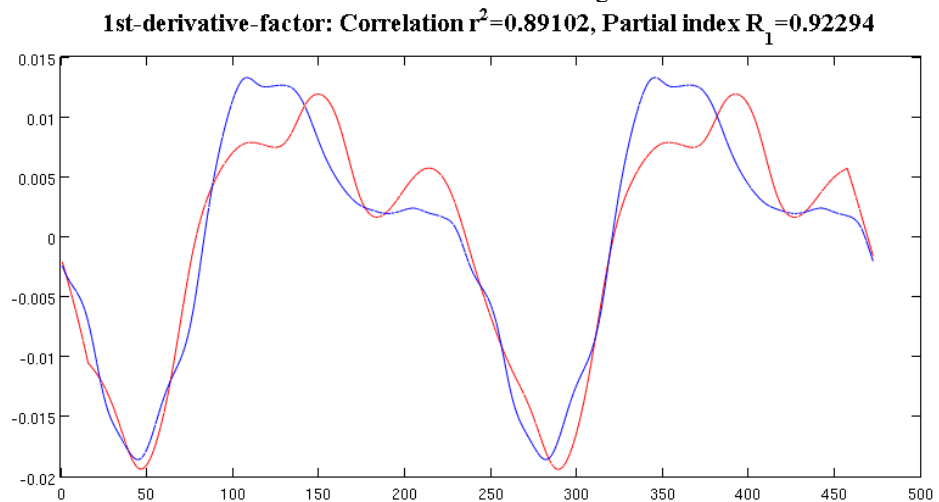


Fig. 56. Correlation of 1st derivative of LV+RV curve obtained by automatic segmentation vs 1st derivative of ensemble averaged FouCG

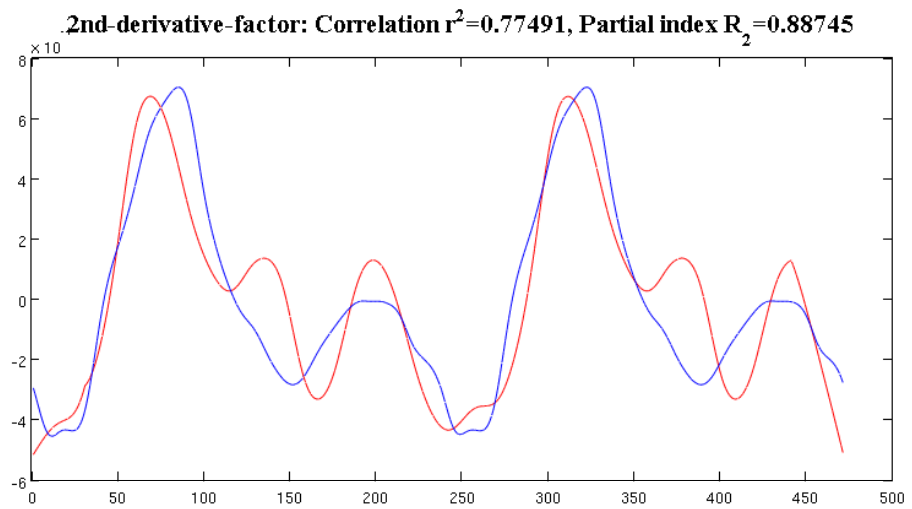


Fig. 57. Correlation of 2nd derivative of LV+RV curve obtained by automatic segmentation vs 2nd derivative of ensemble averaged FouCG

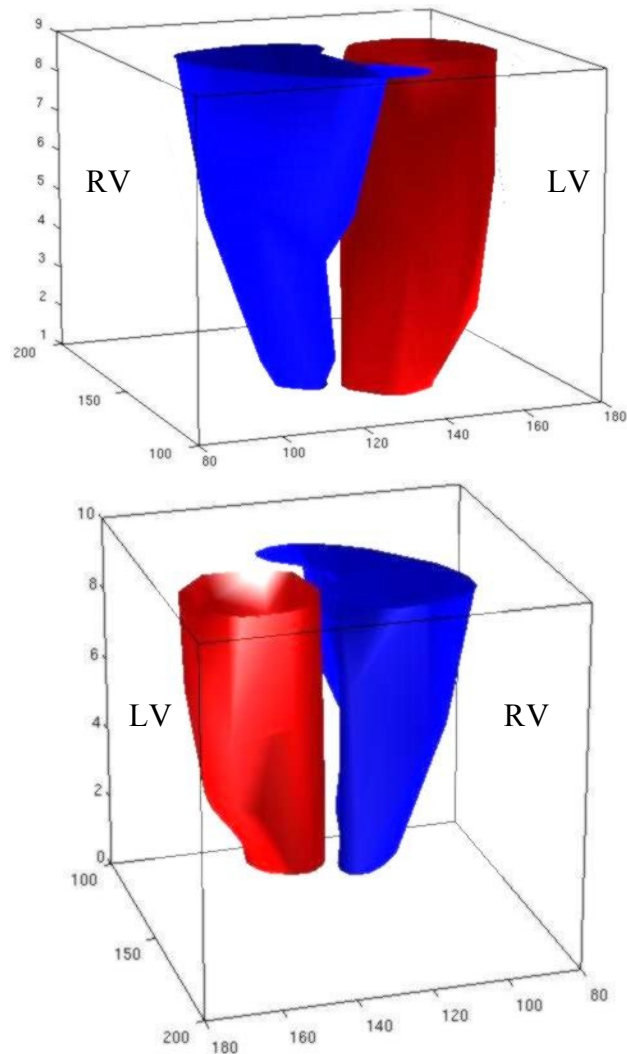


Fig. 58. Reconstructed 3D images of the heart ventricles

9.4 Glossary

Active contours (snakes) – energy-minimizing splines, which are pulled towards desired features of images.

Cardiac index (CI) - a cardiodynamic parameter that relates the cardiac output (Q) to body surface area (BSA). Calculated as $CI = \frac{Q}{BSA}$.

Cardiac output (Q) - the volume of blood being pumped by the heart, in particular by a ventricle in a minute. Calculated as $Q = SV \times HR$.

Ejection fraction (EF) - is the fraction of blood pumped out of ventricles with each heart beat. It is calculated as $EF = \frac{SV}{EDV}$.

End-diastolic volume (EDV) - the volume of blood in a ventricle at the end of filling (diastole).

End-systolic volume (ESV) - the volume of blood in a ventricle at the end of contraction, or systole.

Foucault cardiogram (FouCG) – signal recorded by Foucault cardiograph.

Foucault cardiograph – device for recording electrical bioimpedance, which is used to probe the heart with eddy currents.

Heart rate (HR) - the number of heartbeats per unit of time, typically expressed as beats per minute

Left ventricle (LV) – left ventricle of the heart.

Magnetic resonance imaging (MRI) - medical imaging technique used in radiology to visualize detailed internal structure and limited function of the body.

Right ventricle (RV) – right ventricle of the heart.

Stroke volume (SV) - the volume of blood pumped from one ventricle of the heart with each beat. It is calculated as $SV = EDV - ESV$.